BESIII Analysis Memo

BAM-XXX

May 27, 2024

Study of $J/\psi \to \gamma X(n\bar{n}) \to \gamma n\bar{n}$ at BESIII

Yunlong Xiao[a], Lin Li[b], Yu Zhang[b], Xiao Chu[a], Jianing Guo[a], Liang Yan[a], and Jifeng Hu[b]

[a]*Fudan University, People's Republic of China*
[b]*South China Normal University, People's Republic of China*

Referee Committee

XXX (Chair)[1], XXX[2], XXX[3]

[1]*XXX*
[2]*XXX*
[3]*XXX*

Pubcomm Editors

Editor A[g], Editor B[h]

[g]*Uni. G*
[h]*Uni. H*

HN : *http://hnbes3.ihep.ac.cn/HyperNews/get/paperXXX.html*

Abstract

Using the data samples of $(10087.8 \pm 23.8) \times 10^6$ J/ψ taken with the Beijing Spectrometer (BESIII) at the Beijing Electron-Positron Collider(BEPCII), the decay process $J/\psi \to \gamma n\bar{n}$ has been measured. The branching fraction of $J/\psi \to \gamma X(n\bar{n}) \to \gamma n\bar{n}$ is measured to be $(5.32 \pm 0.20 \pm 0.68) \times 10^{-5}$ for the first time. The ratio of $\frac{Br(J/\psi \to \gamma X(n\bar{n}) \to \gamma n\bar{n})}{Br(J/\psi \to \gamma X(p\bar{p}) \to \gamma p\bar{p})}$ and the difference of $\Delta(M_{X(n\bar{n})} - M_{X(p\bar{p})})$ are calculated to be $0.59 \,^{+0.03}_{-0.08}(stat.) \,^{+0.13}_{-0.34}(syst.)$ and $50.6 \,^{+6.5}_{-19.4}(stat.) \,^{+27.7}_{-27.0}(syst.)$ MeV/c^2. We observe a new resonance, $X(n\bar{n})$, and the mass and width of $X(n\bar{n})$ are measured to be $M_{X(n\bar{n})} = 1882.6 \pm 4.1 \pm 21.0$ MeV/c^2 and $\Gamma_{X(n\bar{n})} = 58.6 \pm 3.7 \pm 18.8$ MeV, respectively.

Contents

1 Introduction

The Standard Model (SM) describes fundamental blocks of matter and their interactions. The fundamental blocks are quarks, leptons, and propagators that interact with each other. In 1964, Gelman and Zweig respectively proposed the quark model of hadron structure, successfully explaining the composition of mesons and baryons [1]. The quark model suggests that mesons are composed of one quark and one anti-quark, and baryons are composed of three quarks, which can well explain the observed particles at that time. Beside conventional mesons and baryons, various types of hadron states are also allowed to exist, including glueball states, hybrid states, and multi-quark states [2,3]. The search and study of these hadron states are one of the cutting-edge topics in high-energy physics. One typical example is X(3872) which is discovered in 2003. Since then, tetraquark and pentaquark states have been observed in experiments such as BABAR [4,5], BELLE [6,7], BESIII [8,9], and LHCb [10,11]. For the six quark state, a deuterium nucleus composed of one proton and one neutron is the only candidate two-nucleon system in nature. Its spin parity is 1^+, and its binding energy is 2.225 MeV [12]. The deuterium nuclei can be produced by strong interaction and other deuterium like two-nucleon states are allowed to exist [13,14]. Baryonium is a special six quark state composed of one baryon and one anti-baryon, for example, $X(p\bar{p})$ or $X(n\bar{n})$. The interaction between them is analogous to that of a baryon pair except differences due to the annihilation effect, attraction, and repulsion potential. Therefore, the study of baryonium will be beneficial for us to understand why other deuterium like two-nucleon states do not exist.

Actually, it is relatively difficult to distinguish exotic particles (including baryonium) from traditional light hadrons. For example, threshold enhancement effect of $p\bar{p}$ invariant mass is firstly observed in the BESII experiment [15] and confirmed in the BESIII and CELO-c experiments via the processes $J/\psi \to \gamma p\bar{p}$ and $\psi(3686) \to \gamma p\bar{p}$ [16,17]. In 2012, the spin parity quantum number of this structure was determined to be $J^{PC} = 0^{-+}$ through partial wave analysis (PWA), where the mass of $X(p\bar{p})$ and width of $X(p\bar{p})$ are measured to be $M = 1832^{+19}_{-5} \pm 19(\text{model})$ MeV/c^2 and $\Gamma \leq 76$ MeV [18], as shown in Table 1. It is puzzling that such strong threshold enhancement was not observed in direct collision cross-section measurements. Therefore, over the last decade there has been a renewed interest in nucleon and anti-nucleon scattering phenomena [19]. Different theories suggest that this structure may come from the bound state of $p\bar{p}$(or baryonium) [20,21], glueball state [22,23], or final state interaction (FSI) [24–26]. However, there is an exception: the enhancement of Λp mass spectra in the process $pp \to p\Lambda K^+$ can not be attributed to Λp bound state [27,28]. We know that these processes J/ψ or $\Upsilon \to \gamma p\bar{p}$, $\pi^0 p\bar{p}$, and $\phi p\bar{p}$, FSI should play a non-negligible role due to the conventional strong nuclear force. However, no similar enhancement was observed in the processes of $J/\psi \to \pi^0 p\bar{p}$ [29], $J/\psi \to \omega p\bar{p}$ [30], $J/\psi \to \phi p\bar{p}$ [31], $\Upsilon \to \gamma p\bar{p}$ [32], and B meson decay [33]. The absence of threshold enhancement effects in these processes

117 does not support the conclusion that the enhancement is entirely due to the FSI.

Tab. 1: The mass and width of $X(p\bar{p})$ from different results

Decay channel	Year	Mass M (MeV/c^2)	Width Γ (MeV)
$J/\psi \to \gamma X(p\bar{p}) \to \gamma p\bar{p}$ [15]	2003	$1859^{+3}_{-10}{}^{+5}_{-25}$	≤ 30
$J/\psi \to \gamma X(p\bar{p}) \to \gamma p\bar{p}$ [17]	2010	$1837^{+10}_{-12}{}^{+9}_{-7}$	0^{+44}_{-0}
$J/\psi \to \gamma X(p\bar{p}) \to \gamma p\bar{p}$ [16]	2010	$1861^{+6}_{-13}{}^{+7}_{-26}$	≤ 38
$J/\psi \to \gamma X(p\bar{p}) \to \gamma p\bar{p}$ [18]	2016	$1832^{+19}_{-5} \pm 19$	≤ 76

118 One possible candidate of the baryonium, $X(1835)$ is firstly discovered in the invariant mass spectrum

119 of ($M\eta'\pi^+\pi^-$) near the $p\bar{p}$ threshold in the process of $J/\psi \to \gamma\eta'\pi^+\pi^-$ by BES collaboration [34],

120 attracts both theoretical and experimental attention as the proton and neutron are the basic components

121 of nucleus. Its mass and width are given as $M = 1833.7 \pm 6.1$ MeV/c^2 and $\Gamma = 67.7 \pm 20.3$ MeV [34]. It

122 was also observed in the BESIII experiment, and in addition, the signal of $X(1835)$ was also observed in

123 invariant mass of $\eta K_S K_S$ via the $J/\psi \to \gamma\eta K_S K_S$ decay channel. Using PWA method, its spin quantum

124 number was determined to be 0^-. For the experimental results of different years, the mass and width

125 of $X(1835)$ are not completely consistent within 3 standard deviations, as shown in Table 2. This raises

126 new question that why the mass and width differences of the observed $X(1835)$ from different decay

127 channels are so significant. Besides, different $X(1835)$ spectrum is that the mass dependence of the $p\bar{p}$

128 spectrum close to the threshold can be explained by the S-wave $p\bar{p}$ FSI in the isospin $I=1$ state within

129 the Watson-Migdal approach [26].

Tab. 2: The mass and width of $X(1835)$ from different results

Decay channel	Year	Mass M (MeV/c^2)	Width Γ (MeV)
$J/\psi \to \gamma\pi^+\pi^-\eta'$ [34]	2005	$1833.7 \pm 6.1 \pm 2.7$	$67.7 \pm 20.3 \pm 7.7$
$J/\psi \to \gamma\pi^+\pi^-\eta'$ [35]	2011	$1836.5 \pm 3.0^{+5.6}_{-2.1}$	$190 \pm 9^{+38}_{-36}$
$J/\psi \to \omega\eta\pi^+\pi^-$ [36]	2011	$1877.3 \pm 6.3^{+3.4}_{-7.4}$	$57 \pm 12^{+19}_{-4}$
$J/\psi \to \gamma\pi^+\pi^-\pi^+\pi^-\pi^+\pi^-$ [37]	2013	$1842.2 \pm 4.2^{+7.1}_{-2.6}$	$83 \pm 14 \pm 11$
$J/\psi \to \gamma\eta K_S K_S$ [38]	2015	$1844 \pm 9^{+16}_{-25}$	$192^{+20}_{-17}{}^{+62}_{-43}$
$J/\psi \to \gamma\pi^+\pi^-\eta'$ [39]	2016	$1825.3 \pm 2.4^{+17.3}_{-2.4}$	$245.2 \pm 13.1^{+4.6}_{-9.6}$
$J/\psi \to \gamma\pi^+\pi^-\eta'$ [39]	2016	$1909.5 \pm 15.9^{+9.4}_{-27.5}$	$273.5 \pm 21.4^{+6.1}_{-64.0}$
$J/\psi \to \gamma\gamma\phi(1020)$ [40]	2018	$1839 \pm 26 \pm 26$	$175 \pm 57 \pm 25$

130 After the observation of the strong near-threshold enhancement of proton and anti-proton $X(p\bar{p})$

131 mass spectrum in $J/\psi \to \gamma p\bar{p}$ decay, lots of theoretical investigations have been available such as new

132 resonance [15], the FSI of $p\bar{p}$ [24–26,41], bound state of $p\bar{p}$ (or baryonium) [20,21], and glueball [22,23].

133 For $X(1835)$, the peak is also observed in $J/\psi \to \gamma\pi^+\pi^-\eta'$ [34], and this is consistent with the previous

measurements in $J/\psi \to \gamma p\bar{p}$ [15]. An updated analysis of $J/\psi \to \gamma\pi^+\pi^-\eta'$ is performed in 2010 [35]. Among these analyses, the locations of the peaks (mass and width of $X(1835)$) are consistent with each other within uncertainties. In 2011, its quantum number was determined to be 0^{-+} [18]. Up to now, this peak has been observed not only in $p\bar{p}$ channel but also in $\pi^+\pi^-\eta'$, $\eta K_S K_S$, $\gamma\phi(1020)$, and $3(\pi^+\pi^-)$ final states with the decay width larger than the former. Therefore, now the question is how to understand this peak in the $\pi^+\pi^-\eta'$, $\eta K_S K_S$, $\gamma\phi(1020)$, and $3(\pi^+\pi^-)$ mass spectrums, whether they are the same stuff as observed from the $p\bar{p}$ case [42]. In experiment, the measurement of $X(n\bar{n})$ can further understand the properties and differences between $X(p\bar{p})$, $X(n\bar{n})$, and $X(1835)$.

So far, the study of neutron and anti-neutron through radiation decay has always been missing. The proton and neutron are isospin doublet. The different isospin third components and the influence of Coulomb interaction reflect the different behavior of nucleon and anti-nucleon in different theoretical calculations. Assuming that both $p\bar{p}$ and $n\bar{n}$ are decayed from the same baryonium, then the yields of $J/\psi \to \gamma X(p\bar{p}) \to \gamma p\bar{p}$ and $J/\psi \to \gamma X(n\bar{n}) \to \gamma n\bar{n}$ are very close. Assuming pure FSI in the $p\bar{p}$ or $n\bar{n}$ system, and only considering the contribution of isospin 0 and 1 of $1S^0$, based on the isospin coupling coefficient, and measurement results of proton and anti-proton, it can be expected that the yield near the threshold of neutron and anti-neutron is about half of that of proton and anti-proton [26]. Therefore, by comparing experiments, we can effectively test the reliability of multiple theories and provide strong experimental data for studying baryonium. In this context, it is of great significance to understand and determine the properties of $X(1835)$, $X(p\bar{p})$, and $X(n\bar{n})$ by studying the threshold effect of neutron and anti-neutron through J/ψ radiation decay, as well as to further investigate the enhancement in the threshold of proton and anti-proton production. Recently, the J/ψ data of 10 billion taken with the Beijing Spectrometer (BESIII) at the Beijing Electron-Positron Collider (BEPCII) provides a unique opportunity to study the production and decay of nucleon and anti-nucleon system. Moreover, our understanding of detector and the introduction of advanced research method can effectively distinguish and measure neutron and anti-neutron.

2 The BEPCII and BESIII detector

The BESIII detector [43] records symmetric e^+e^- collisions provided by the BEPCII storage ring [44], which operates with a peak luminosity of 1×10^{33} cm^{-2}s^{-1} in the center of mass energy range from 2.0 to 4.9 GeV. BESIII has collected large data samples in this energy region [45]. The cylindrical core of the BESIII detector covers 93% of the full solid angle and consists of a helium-based multilayer drift chamber (MDC), a plastic scintillator time-of-flight system (TOF), and a CsI(Tl) electromagnetic calorimeter (EMC), which are all enclosed in a superconducting solenoidal magnet providing a 1.0 T (0.9 T in 2012) magnetic field. The solenoid is supported by an octagonal flux-return yoke with resistive plate counter muon identification modules interleaved with steel. The charged-particle momentum resolution at 1 GeV/c is 0.5%, and the dE/dx resolution is 6% for electrons from Bhabha scattering. The EMC measures photon energies with a resolution of 2.5% (5%) at 1 GeV in the barrel (end cap) region. The time resolution in the TOF barrel region is 68 ps, while that in the end cap region is 110 ps. The end cap TOF system was upgraded in 2015 using multi-gap resistive plate chamber technology, providing a time resolution of 60 ps [46].

3 Data sets and Monte Carlo Simulation

3.1 Data

The data consists of $(10087.8 \pm 23.8) \times 10^6 \, J/\psi$ events collected with the BESIII detector during 2009, 2012, 2017, and 2018 years [54].

3.2 Monte Carlo Simulation

Monte Carlo simulation samples are produced with the GEANT4-based [47] packages which model the description of the BESIII detector and mimic its response to various particles. The J/ψ samples are simulated with the KKMC generator [48], which is an event generator based on precise predictions of the Electroweak Standard Model. The beam energy spread and initial state radiation (ISR) are taken into account in the simulation. The software framework used for the data analysis is BOSS(BESIII Offline Software System), which is developed from Gaudi. This work is under BOSS version 7.0.8, which is shown in Table 3. An inclusive sample consisting of simulated $10000 \times 10^6 \, J/\psi$ events are used to investigate possible backgrounds. The known decay modes are modelled with EVTGEN [49] using branching fractions taken from the Particle Data Group [51], and the remaining unknown charmonium decays are modelled with LUNDCHARM [50]. Final state radiation (FSR) from charged final state particles is incorporated using the PHOTOS package.

In addition, signal MC samples are used to determine the selection efficiency of the signal process, and to optimize our selection criteria. Other exclusive samples of $J/\psi \to \pi^0 n\bar{n} \to \gamma\gamma n\bar{n}$, $J/\psi \to \eta n\bar{n} \to \gamma\gamma n\bar{n}$, $J/\psi \to \gamma\pi^0\pi^0 \to \gamma\gamma\gamma\gamma$, and $J/\psi \to \gamma K_L K_L$ are used to study major background, as listed in Table 4. Single particle MC including γ, n, and $\bar{n}$ is used to perform the training BDT, as listed in Table 4.

Tab. 3: J/ψ data sets collected at BESIII, the number of events of J/ψ, and the BOSS version.

Collected J/ψ in different years	Number of events	Boss Version
J/ψ (2009)	224.0 ± 1.3 M	7.0.8
J/ψ (2012)	1088.5 ± 4.4 M	7.0.8
J/ψ (2017 − 2019)	8774.0 ± 39.4 M	7.0.8

Tab. 4: Exclusive MC samples, the decay mode, the number of events, and the surviving events.

Category	Generate mode	Number of events	Surviving events(After normalization)
$J/\psi \to \gamma n\bar{n}$	PHSP	8 Million	–
$J/\psi \to \pi^0 n\bar{n} \to \gamma\gamma n\bar{n}$	PHSP	4 Million	–
$J/\psi \to \eta n\bar{n} \to \gamma\gamma n\bar{n}$	PHSP	2 Million	–
$J/\psi \to \gamma\pi^0\pi^0 \to \gamma\gamma\gamma\gamma\gamma$	PHSP	8 Million	3
$J/\psi \to \gamma K_L K_L$	PHSP	8 Million	89
γ	PHSP	20 Thousand	–
n	PHSP	20 Thousand	–
$\bar{n}$	PHSP	20 Thousand	–

4   Event Selections

The final state of the signal process $J/\psi \to \gamma X(n\bar{n}) \to \gamma n\bar{n}$ contains two neutrally charged hadrons and one photon. Since the BESIII detector doesn't have a hadronic calorimeter, the neutron and antineutron are reconstructed and identified with the EMC and TOF detectors.

4.1   Track selection

4.1.1   Selections of charged tracks in the MDC

- One event with any charged trackers are rejected, i.e., N(trk) = 0. Charged tracks reconstructed by multi-layer chamber (MDC) hit information must be fitted by Kalman method successfully and came from the interaction region in three dimensions. Due to changing beam conditions, the interaction point (IP) moves. Thus, a separate average IP is determined for each run using the VertexDbSvc package. Events with charged tracks are rejected since signal process $J/\psi \to \gamma n\bar{n}$ has no charged track.

4.1.2   Selections of showers in the EMC

- $E \geq 25$ MeV in the barrel region ($|\cos\theta| < 0.80$) and $E \geq 50$ MeV in the end cap region ($0.86 < |\cos\theta| < 0.92$). The deposited energy of each shower in the EMC must be more than 25 MeV in the barrel region and more than 50 MeV in the end cap region.

- $N_{\rm s} \geq 3$. The signal process $J/\psi \to \gamma X(n\bar{n}) \to \gamma n\bar{n}$ is reconstructed using at least three good showers in the EMC detector.

4.2   Photon, neutron, and anti-neutron reconstruction

The multiple variable analysis (MVA) is used, and the boosted decision tree (BDT) is applied to distinguish photon, anti-neutron, and neutron. Corresponding variables of showers are shown in Table 5. The information of photon, neutron, and anti-neutron on the EMC detector can be obtained by matching the MC truth information. In this way, training samples related to photon, neutron, and anti-neutron candidates are prepared.

Tab. 5: The variables of the shower energy, shower shape, new-var1, new-var2, and new-var3, used in MVA analysis and their category and description.

Variable	Category	Description
shower energy	Shower energy	Total energy observed in EMC
shower dtheta	Shower shape	Error of shower angle
shower dphi	Shower shape	Error of shower angle
shower dE	Shower energy	Error of shower energy
shower secondMoment	Shower shape	Second moment of shower shape
shower latMoment	Shower shape	Lateral moment of shower shape
shower a20Moment	Shower shape	a20 moment of shower shape
shower a42Moment	Shower shape	a42 moment of shower shape
shower hitnumber	Shower shape	Number of crystals in the shower
e3x3	Shower energy	total energy of 3×3 crystal around seed
e5x5	Shower energy	total energy of 5×5 crystal around seed
shower eSeed	Shower energy	energy of seed
new var1	(e5x5-e3x3)/e5x5	−
new var2	(e3x3-shower eSeed)/e3x3	−
new var3	(showerenergy-showereSeed)/((hitnumber-1)*eSeed)	−

4.2.1 Photon reconstruction

Using the new-var1, new-var2, new-var3, secondMoment, latMoment, a20Moment, a42Moment, and nhits (numbers of hits) information in the EMC, photon candidate is classified via the BDT method. Here, other variables of shower energy, shower dtheta, shower dphi, shower dE, e3x3, and e5x5 are not used in this method since they are strongly correlated with the true energy of photon to further avoid bias. The output discriminator of BDT training is shown in Figure 1. The discriminator value for the BDT is evaluated by optimization of $S/\sqrt{S+B}$ with a signal to background ratio setting at 1:2, while -0.04 is taken in our analysis. Here, S denotes the number of photon shower, and B denotes the number of neutron shower and anti-neuron shower.
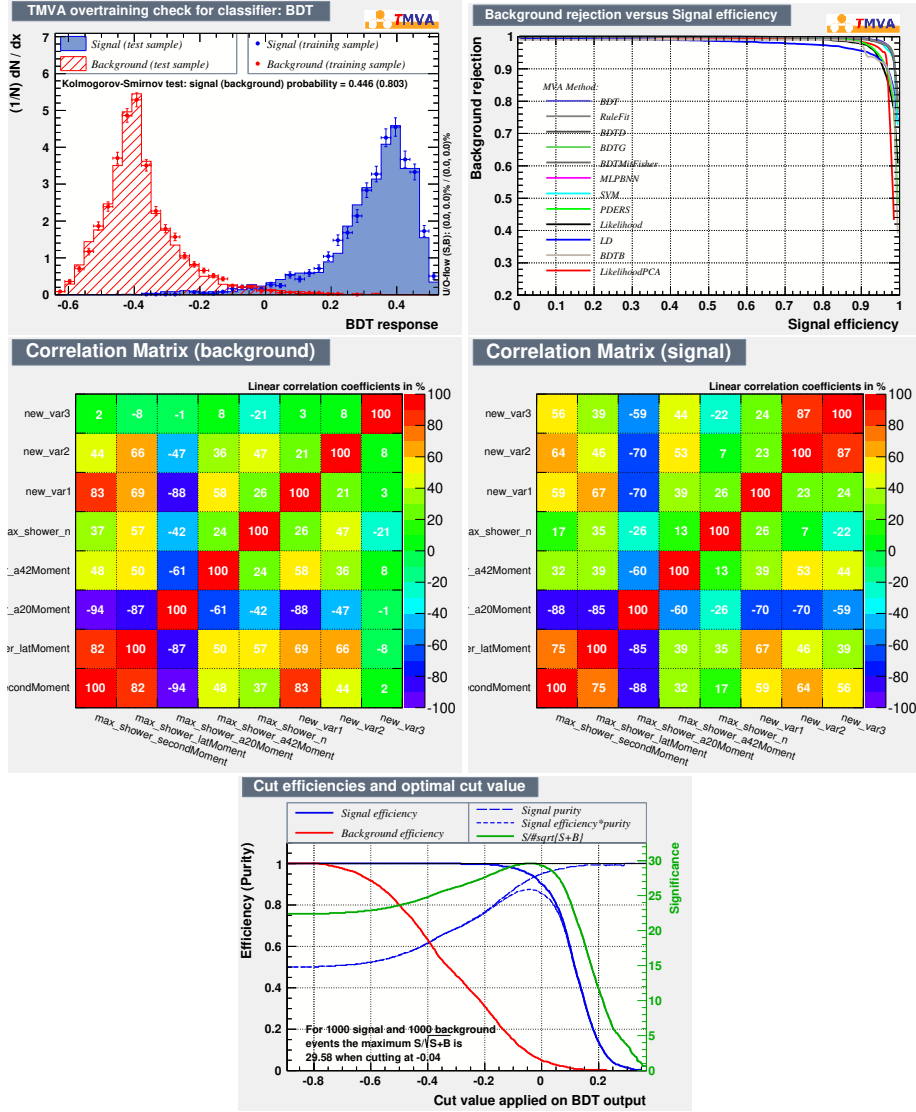
Fig. 1: Output discriminator of BDT training. The blue dots are the likelihood output from signal MC training sample, the blue histogram is the likelihood output from the signal MC test sample, the red dots are the likelihood output from background training sample and the red histogram is the likelihood output from the background test sample. (upper right) The background rejection versus signal efficiency. (middle left) Correlation matrix for signal MC variables. (middle right) correlation matrix for background. (bottom) The figure-of-merit for BDT selection.

4.2.2 Neutron reconstruction

Using the shower energy, shower dtheta, shower dphi, shower dE, secondMoment, latMoment, a20Moment, a42Moment, nhits (numbers of hits), e3x3, e5x5, shower eSeed, new-var1, new-var2, and new-var3 information in the EMC, neutron candidate is classified via the BDT method. The output discriminator of BDT training is shown in Figure 2. The discriminator value for the BDT is evaluated by optimization of $S/\sqrt{S + B}$ with a signal to background ratio setting at 1:2, while -0.03 is taken in our

233 analysis. Here, S denotes the number of photon shower, and B denotes the number of neutron shower
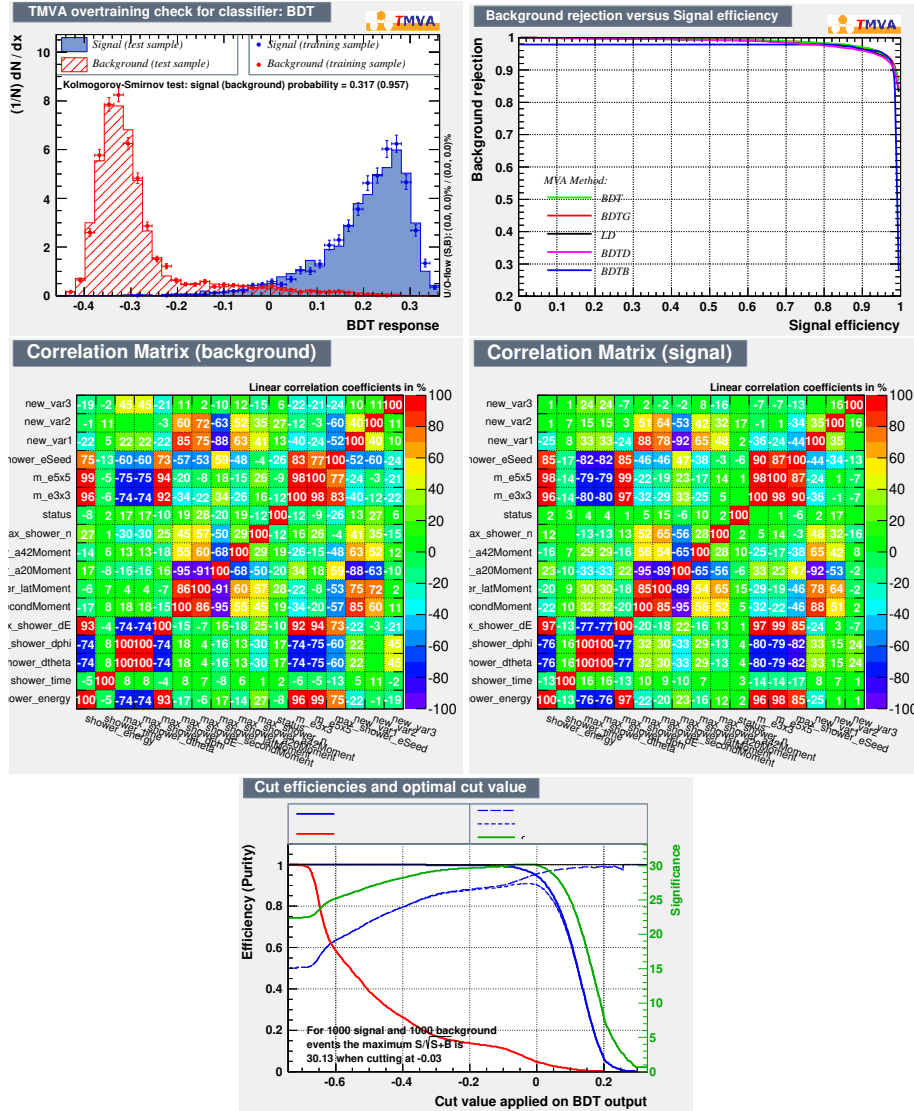
234 and anti-neuron shower.

Fig. 2: Output discriminator of BDT training. The blue dots are the likelihood output from signal MC training sample, the blue histogram is the likelihood output from the signal MC test sample, the red dots are the likelihood output from background training sample and the red histogram is the likelihood output from the background test sample. (upper right) The background rejection versus signal efficiency. (middle left) Correlation matrix for signal MC variables. (middle right) correlation matrix for background. (bottom) The figure-of-merit for BDT selection.

4.2.3 Anti-neutron reconstruction

236 Using the shower energy, shower dtheta, shower dphi, shower dE, secondMoment, latMoment,

237 a20Moment, a42Moment, nhits (numbers of hits), e3x3, e5x5, shower eSeed, new-var1, new-var2, and

238 new-var3 information in the EMC, anti-neutron candidate is classified via the BDT method. The output

discriminator of BDT training is shown in Figure 3. The discriminator value for the BDT is evaluated by optimization of $S/\sqrt{S+B}$ with a signal to background ratio setting at 1:2, while -0.04 is taken in our analysis. Here, S denotes the number of anti-neuron shower, and B denotes the number of photon shower and neutron shower.
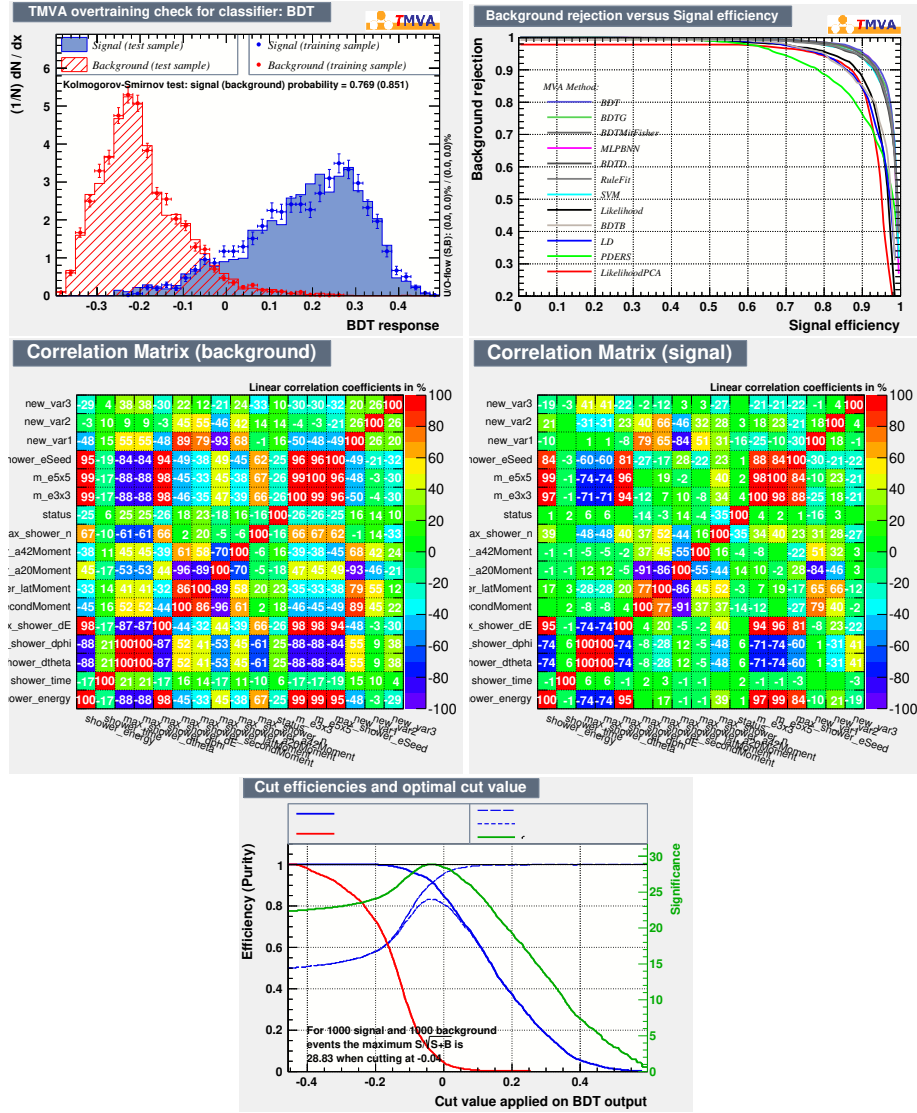

Fig. 3: Output discriminator of BDT training. The blue dots are the likelihood output from signal MC training sample, the blue histogram is the likelihood output from the signal MC test sample, the red dots are the likelihood output from background training sample and the red histogram is the likelihood output from the background test sample. (upper right) The background rejection versus signal efficiency. (middle left) Correlation matrix for signal MC variables. (middle right) correlation matrix for background. (bottom) The figure-of-merit for BDT selection.

4.3 Energy difference

The distribution of the absolute value of the energy difference between neutron and anti-neutron ΔE is shown in Figure 4 (left) and it is optimized based on the figure of merit (right). In the plot, S denotes signal MC, which has been scaled to luminosity of data via our measurement of branching fraction, and B denotes the backgrounds from the inclusive MC. In order to further remove potential background contribution, such as $J/\psi \to n\bar{n}$, $J/\psi \to \gamma\eta'(\eta' \to \pi^0\pi^0\eta, \eta \to \gamma\gamma)$, $J/\psi \to \pi^0 K_L K_S$, and $J/\psi \to \pi^0\pi^0\gamma$, the ΔE is required to be less than 0.22 GeV.
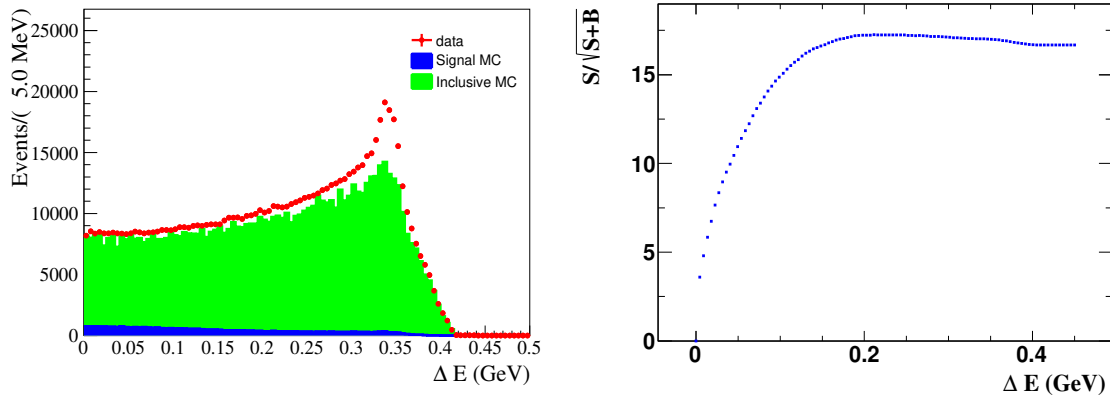

Fig. 4: (left) The ΔE distributions of energy difference between neutron and anti-neutron. The red dots with error bars represent data. The green line and blue line represent the inclusive MC and signal MC, respectively. (right) Figure of merit for the ΔE, where S is signal MC, and B is the backgrounds from the inclusive MC.

4.4 Maximum unused energy deposition

The maximum unused deposition energy means maximum energy of shower in the EMC after excluding photon, neutron, and anti-neutron candidates. The distribution of maximum deposition energy is shown in Figure 5 on the left and it is optimized based on the figure of merit as shown in Figure 5 on the right. In the plot, S is signal MC, which has been scaled to luminosity of data via our measurement of branching fraction, and B is the backgrounds from the inclusive MC. In order to further remove potential background contribution, such as $J/\psi \to \pi^0 n\bar{n}$, $J/\psi \to \eta n\bar{n}$, $J/\psi \to \pi^0 K_L K_S$, and $J/\psi \to \pi^0\pi^0\gamma$, so we require the maximum deposition energy is less than 0.19 GeV.
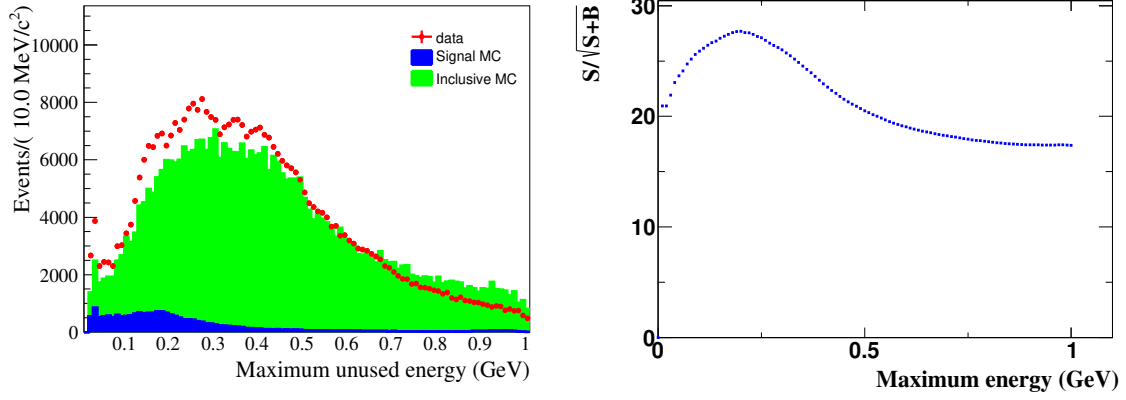
Fig. 5: (left) The distribution of the maximum unused deposition energy of shower in the EMC. The red dots with error bars represent data. The green line and blue line represent the inclusive MC and signal MC, respectively. (right) Figure of merit for the maximum unused deposition energy, where S is signal MC, and B is the backgrounds from the inclusive MC.

4.5 Kinematic fitting using two constraints

Using the neutron and anti-neutron position measured in the EMC and the kinematic fitting method, we can calculate the three-momentum of neutron and anti-neutron and obtain invariant mass of $n\bar{n}$. The background contributions $J/\psi \rightarrow \pi^0 n\bar{n}$, $J/\psi \rightarrow \eta n\bar{n}$, $J/\psi \rightarrow \gamma\pi^0\pi^0$, and $J/\psi \rightarrow \gamma K_L K_L$, $J/\psi \rightarrow \pi^0(\pi^0 \rightarrow \gamma\gamma)K_L K_S(K_S \rightarrow \pi^0\pi^0, \pi^0 \rightarrow \gamma\gamma)$, and other non-$\gamma n\bar{n}$ final states can be suppressed. Here, a four-constraint-energy-momentum conservation kinematic fitting is performed for $\gamma n\bar{n}$ candidates. In the kinematic fitting, the energies of n and $\bar{n}$ are missing. Therefore, the constraints of kinematic fitting are $(4-1-1) = 2C$. This χ^2_{2C} value is optimized based on the figure of merit as shown in Figure 6. In the plot, S is signal MC, and B is the backgrounds from the inclusive MC. Besides, the signal MC has been scaled to luminosity of data via our measurement of branching fraction. Therefore, a requirement on the quality of the 2C kinematic fitting $\chi^2_{2C} \leq 15$ is imposed.
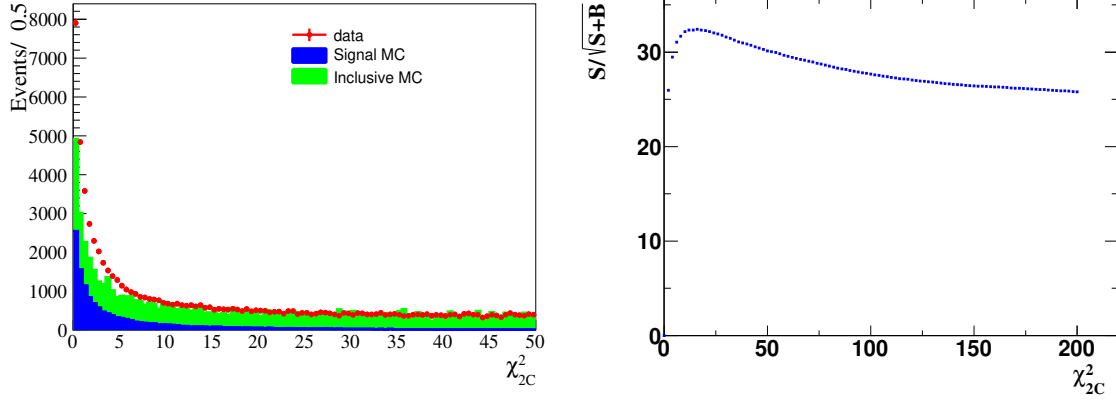
Fig. 6: (left) The χ^2_{2C} distribution for $J/\psi \to \gamma n\bar{n}$. The red dots with error bars represent data. The green line and blue line represent the inclusive MC and signal MC, respectively. (right) Figure of merit for the χ^2_{2C} , the figures is for $J/\psi \to \gamma n\bar{n}$, where S is signal MC, and B is the backgrounds from the inclusive MC.

4.6 Kinematic fitting by swapping neutron-photon hypothesis

In our analysis, in order to remove error combination between photon and neutron candidates, we performed kinematic fitting of the error combination, and require that the status of kinematic fitting should be unsuccessful. In kinematic fitting of the error combination, for the photon candidate, photon is assigned neutron mass (0.93956 GeV/c^2), and for the neutron candidate, neutron is assigned photon mass (0.0 GeV/c^2).

4.7 Kinematic fitting by comparing signal-background hypothesis

To further remove potential backgrounds $J/\psi \to \pi^0 n\bar{n}$, $J/\psi \to \eta n\bar{n}$, and $J/\psi \to \gamma K_L K_L$, a two-constraint-energy-momentum conservation kinematic fitting is performed, and requirement on the quality of the background $\chi^2_{\text{bkg 2C}}$ value is required to be larger than signal χ^2_{2C} value.

4.8 π^0 mass window

In order to further remove background contributions and improve the mass resolution, we apply a veto on the defined $\gamma\gamma$ mass spectra. We fit these defined mass spectra of inclusive MC sample, where it is described by a double gaussian function, and the mass window [0.11, 0.16] GeV/c^2 is defined within 3 σ range in the Figure 7. Here, the background processes of $J/\psi \to \pi^0\gamma\gamma$, $J/\psi \to \pi^0 n\bar{n}$, $J/\psi \to \pi^0\pi^0\pi^0\gamma$, $J/\psi \to \pi^0 K_L K_S(K_S \to \pi^0\pi^0)$, and $J/\psi \to \pi^0\pi^0\omega$ and other involving π^0 final sate can be also suppressed.
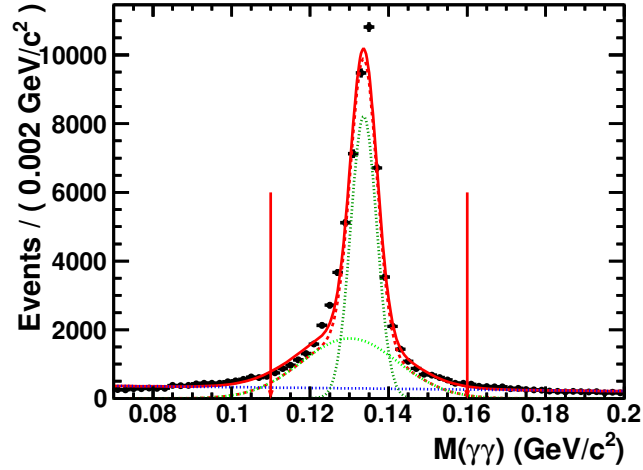
Fig. 7: The distribution of $M(\gamma\gamma)$ for the inclusive MC. The black dots with error bars are the inclusive MC, the red solid line is the total fitting function, the red dashed line is the background contribution containing π^0 final state, and the blue dotted line is the background contribution of non-π^0 final state.

4.9 Anti-neutron selection using time information

The J/ψ inclusive samples are used to study background level, and the main background contributions include $J/\psi \rightarrow \pi^0 n\bar{n}$, $J/\psi \rightarrow \eta n\bar{n}(\eta \rightarrow \gamma\gamma)$, $J/\psi \rightarrow \pi^0 K^0 \bar{K}^0 (K^0 \rightarrow K_L^0, \bar{K}^0 \rightarrow K_L^0)$, and $J/\psi \rightarrow \pi^0 \pi^0 \gamma$ processes, as shown in Table 6. So, the Tof selection of anti-neutron is used to further suppress background contributions.

Tab. 6: Topology of background in generic J/ψ inclusive MC sample.

rowNo	decay tree	decay final state	iDcyTr	nEtr	nCEtr
1	$J/\psi \rightarrow \pi^0 n\bar{n}$	$\pi^0 n\bar{n}$	3	731	731
2	$J/\psi \rightarrow n\bar{n}\gamma$	$n\bar{n}\gamma$	2	480	1211
3	$J/\psi \rightarrow \eta n\bar{n}, \eta \rightarrow \gamma\gamma$	$n\bar{n}\gamma\gamma$	1	220	1431
4	$J/\psi \rightarrow \pi^0 K^0 \bar{K}^0, K^0 \rightarrow K_L^0, \bar{K}^0 \rightarrow K_L^0$	$\pi^0 K_L^0 K_L^0$	0	84	1515
5	$J/\psi \rightarrow \pi^0 \pi^0 \gamma$	$\pi^0 \pi^0 \gamma$	16	57	1572
6	$J/\psi \rightarrow f_4(2050)\gamma, f_4(2050) \rightarrow \pi^0 \pi^0$	$\pi^0 \pi^0 \gamma$	10	54	1626
7	$J/\psi \rightarrow n\bar{n}$	$n\bar{n}$	13	33	1659
8	$J/\psi \rightarrow f_0(1710)\gamma, f_0(1710) \rightarrow K^0 \bar{K}^0, K^0 \rightarrow K_L^0, \bar{K}^0 \rightarrow K_L^0$	$K_L^0 K_L^0 \gamma$	11	30	1689
9	$J/\psi \rightarrow f_2'\gamma, f_2' \rightarrow K_L^0 K_L^0$	$K_L^0 K_L^0 \gamma$	15	29	1718
10	$J/\psi \rightarrow f_0(1710)\gamma, f_0(1710) \rightarrow \pi^0 \pi^0$	$\pi^0 \pi^0 \gamma$	14	22	1740
11	$J/\psi \rightarrow f_2(1270)\gamma, f_2(1270) \rightarrow \pi^0 \pi^0$	$\pi^0 \pi^0 \gamma$	18	22	1762
12	$J/\psi \rightarrow \pi^0 K_L^0 K_S^0, K_S^0 \rightarrow \pi^0 \pi^0$	$\pi^0 \pi^0 \pi^0 K_L^0$	12	8	1770
13	$J/\psi \rightarrow \pi^0 K^0 \bar{K}^*, K^0 \rightarrow K_L^0, \bar{K}^* \rightarrow \pi^0 \bar{K}^0, \bar{K}^0 \rightarrow K_L^0$	$\pi^0 \pi^0 K_L^0 K_L^0$	4	8	1778
14	$J/\psi \rightarrow f_4(2050)\gamma, f_4(2050) \rightarrow K_L^0 K_L^0$	$K_L^0 K_L^0 \gamma$	5	8	1786
15	$J/\psi \rightarrow f_2(1640)\gamma, f_2(1640) \rightarrow K_L^0 K_L^0$	$K_L^0 K_L^0 \gamma$	19	8	1794

rowNo	decay tree	decay final state	iDcyTr	nEtr	nCEtr
16	$J/\psi \to \eta'\gamma, \eta' \to \gamma\gamma$	$\gamma\gamma\gamma$	27	7	1801
17	$J/\psi \to \eta_c\gamma, \eta_c \to \pi^0 K^0 \bar{K}^0, K^0 \to K_L^0, \bar{K}^0 \to K_L^0$	$\pi^0 K_L^0 K_L^0 \gamma$	36	7	1808
18	$J/\psi \to \pi^0\pi^0\omega, \omega \to \pi^0\gamma$	$\pi^0\pi^0\pi^0\gamma$	46	7	1815
19	$J/\psi \to \pi^0\pi^0\pi^+\pi^-$	$\pi^0\pi^0\pi^+\pi^-$	25	6	1821
20	$J/\psi \to \eta'\gamma, \eta' \to \pi^0\pi^0\eta, \eta \to \gamma\gamma$	$\pi^0\pi^0\gamma\gamma\gamma$	30	6	1827

The flight times of photon, neutron and K_L particle satisfy the condition: $T(\gamma) < T(K_L) < T(n) \approx T(\bar{n})$. Therefore, based on the property in the TOF, it can effectively separate signal anti-neutrons from photons or K_L in the background processes, and other background processes of $J/\psi \to \gamma\pi^0\pi^0$, $J/\psi \to \gamma K_L K_L$, $J/\psi \to \pi^0(\pi^0 \to \gamma\gamma)K_L K_S (K_S \to \pi^0\pi^0, \pi^0 \to \gamma\gamma)$ can be further suppressed. Here, the ΔT is defined with: $\Delta T = T_{\text{tof}} - T_s - T_p$, where T_{tof} is the measured time of the TOF, T_s is the event start time of anti-neutron, and T_p is the predicted flight time from interaction point (IP) to TOF counters, which is determined by formula l/c, where l is the distance from IP to TOF counters and c is velocity of light. Figure 8 shows the $T_{\text{tof}} - T_s - T_p$ spectrum, which has a significant peak at zero. The peak is dominated by processes with photons in the final state. In order to select anti-neutron, and suppress photon and K_L state, the ΔT window is required to be within $\Delta T \in (2, 7.6)$ ns or $\Delta T \in (8.5, 15)$ ns. After ΔT requirement, the $J/\psi \to \gamma\pi^0\pi^0$(or other pure γ final states) and $J/\psi \to \gamma K_L K_L$(or other including K_L final states) contribution are reduced by 139 and 4 times. However, the signal process $J/\psi \to \gamma n\bar{n}$ contribution is only reduced 1.2 times.

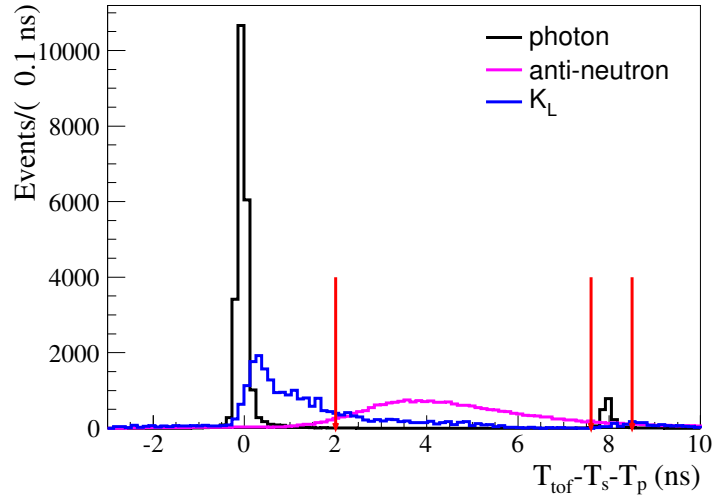Fig. 8: The time difference ΔT between the measured time of shower and expected time of photon. The dark, blue, and red line represent the time of the photon, K_L, and anti-neutron, respectively. The red arrows are defined as time windows.

5 Measurement of mass, width, and branching fraction

5.1 Selection validation

We compared the distributions of several observable using MC samples, at both the event generator level and the reconstruction level, as shown in Figure 9. We check the coincidence between reconstructed shower positions in the EMC and the truth momentum for three neutrally charged particles, as shown in Figure 10. From these plots, we see that selections discussed in the previous section work well.
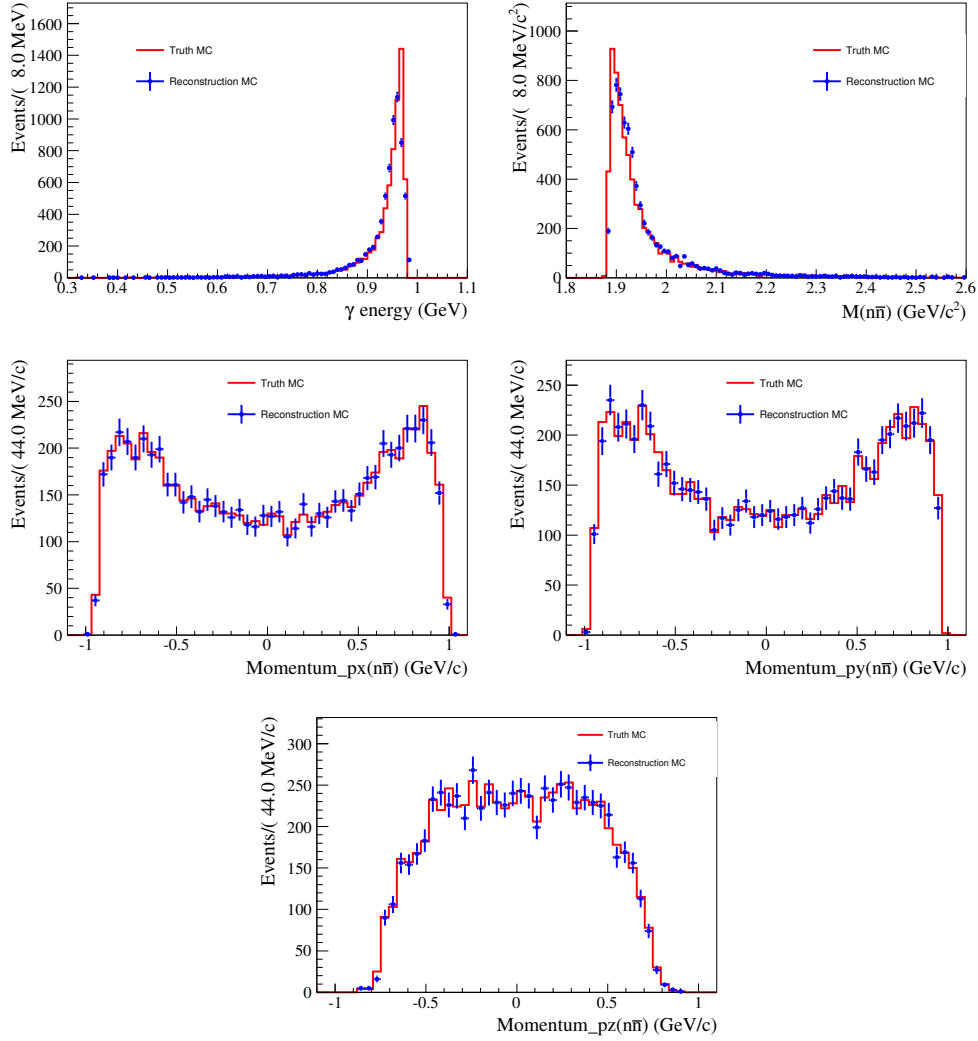

Fig. 9: The photon energy, invariant mass $n\bar{n}$, three-momentum of $n\bar{n}$ distributions comparison. The blue and red lines represent the distributions of truth MC and reconstructed MC for the photon energy (upper left), invariant mass of $n\bar{n}$ (upper right), the three-momentum of $n\bar{n}$ (middle and bottom), respectively.
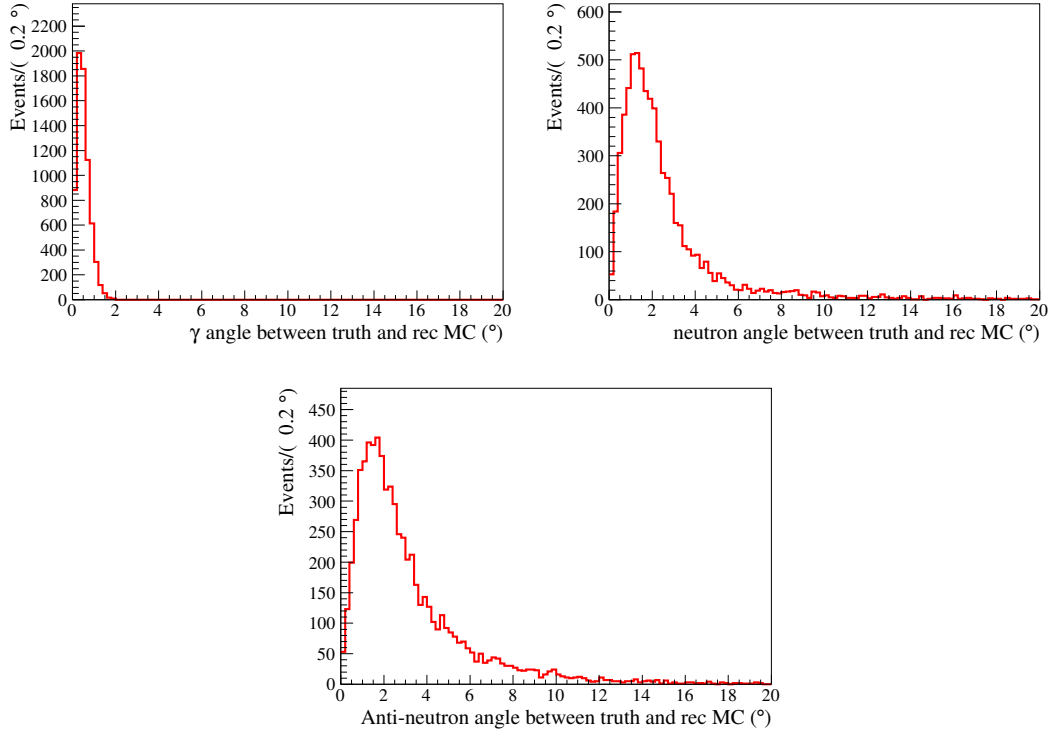
Fig. 10: The photon, neutron, and anti-neutron angle distributions between truth and reconstruction MC. The red lines represent the angle distributions of (photon, neutron, and anti-neutron) the flight direction between truth MC and reconstruction MC.

5.2 Some comparison between data and MC

We draw more distributions including main background and signal events based on the J/ψ inclusive and exclusive MC samples, as the Figure 11. The dominant peaking background channels are $J/\psi \rightarrow \gamma f_0(2100) \rightarrow \gamma n\bar{n}$, $J/\psi \rightarrow \gamma f_2(1910) \rightarrow \gamma n\bar{n}$, $J/\psi \rightarrow \gamma n\bar{n}$, $J/\psi \rightarrow \eta n\bar{n}$, and $J/\psi \rightarrow \pi^0 n\bar{n}$, which are scaled based on branching fraction and selection efficiency. MC simulations can roughly describe data sample.
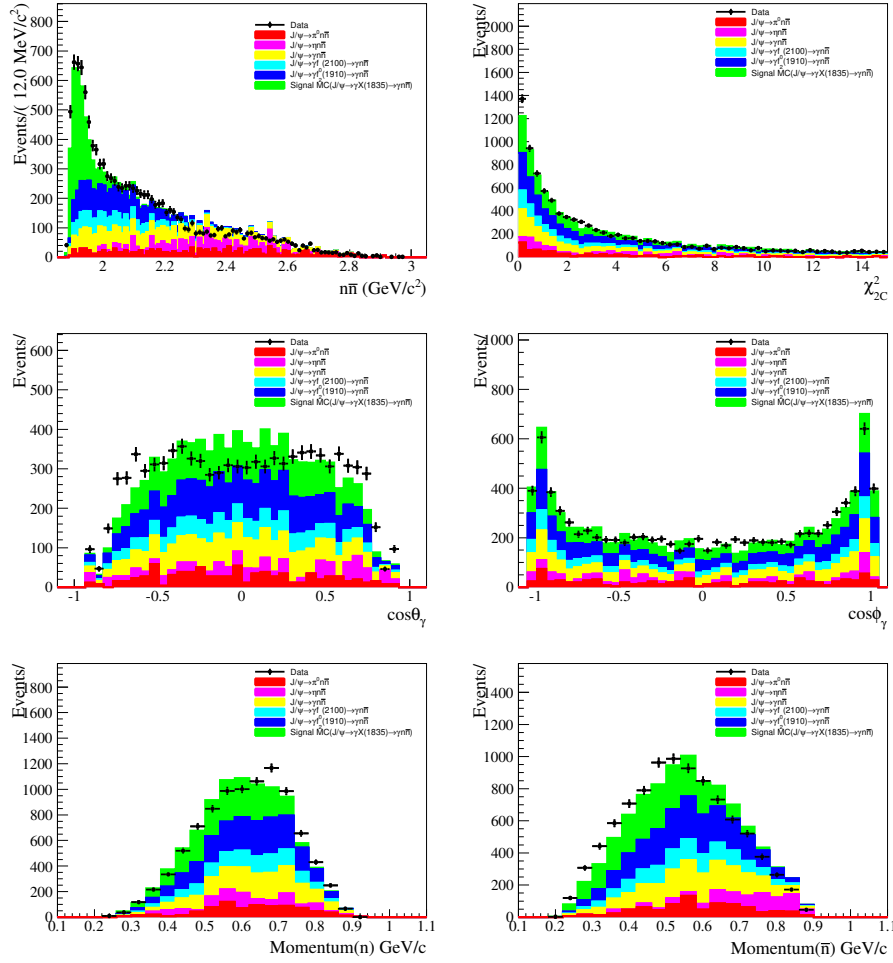
Fig. 11: The invariant mass of $n\bar{n}$, χ^2_{2C}, $\cos\theta_\gamma$, $\cos\phi_\gamma$, n momentum, and $\bar{n}$ momentum distributions. The green, blue, light blue, yellow, light red, and red histograms represent signal channel, $J/\psi \to \gamma f_0(2100) \to \gamma n\bar{n}$, $J/\psi \to \gamma f_2(1910) \to \gamma n\bar{n}$, $J/\psi \to \gamma n\bar{n}$, $J/\psi \to \eta n\bar{n}$, and $J/\psi \to \pi^0 n\bar{n}$ contributions.

5.3 MC efficiency correction

The response of neutrons and anti-neutrons to the detector simulated by the Geant4 software packages, are known to lack sufficient accuracy. To determine the precise branching fraction, mass, and width, the correction of selection efficiency is performed with control samples of the processes $J/\psi \to p\bar{n}\pi^-$ and $J/\psi \to \bar{p}n\pi^+$ (see also details in Appendix). Two dimensional efficiencies along with different momenta and polar angles are considered. Here, the efficiency differences between data and MC are classified as three categories: the selection efficiencies of neutron and anti-neutron in the EMC detector, the selection efficiencies of neutron and anti-neutron by using BDT method, and the selection efficiency of anti-neutron in the TOF detector, as shown in Figure 12, Figure 13, and Figure 14. For example, the flowchart for efficiency correction of the BDT method is shown as Figure 15.
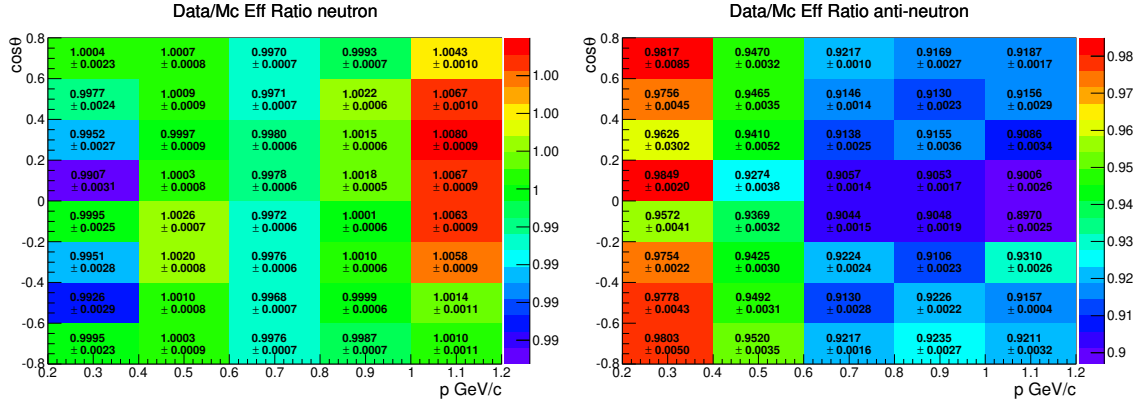
Fig. 12: The ratio of selection efficiency (Data/MC) corresponding to EMC selections (left: neutron, right: anti-neutron).
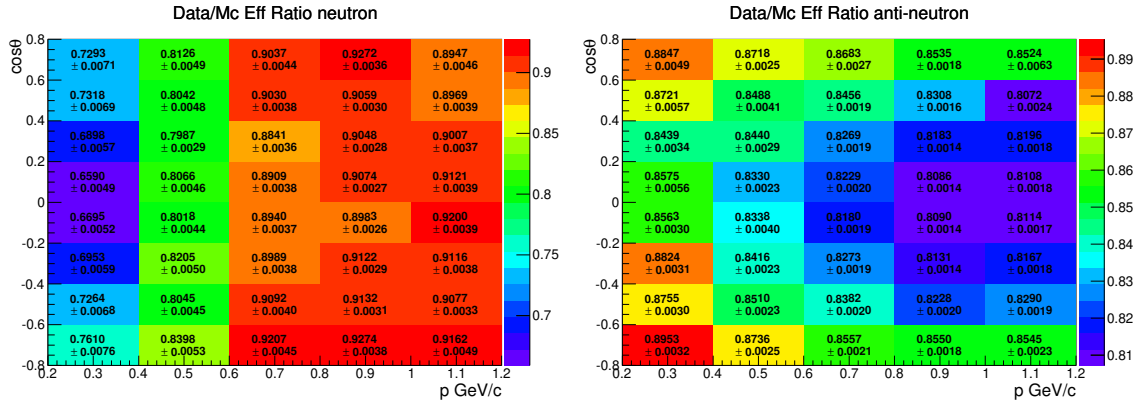

Fig. 13: The ratio of selection efficiency (Data/MC) corresponding to BDT selections (left: neutron, right: anti-neutron).
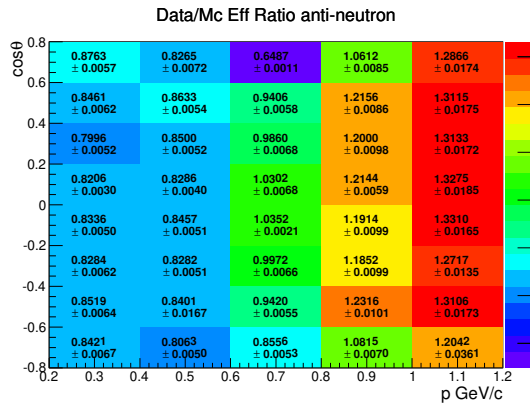

Fig. 14: The ratio of selection efficiency (Data/MC) corresponding to TOF selections.
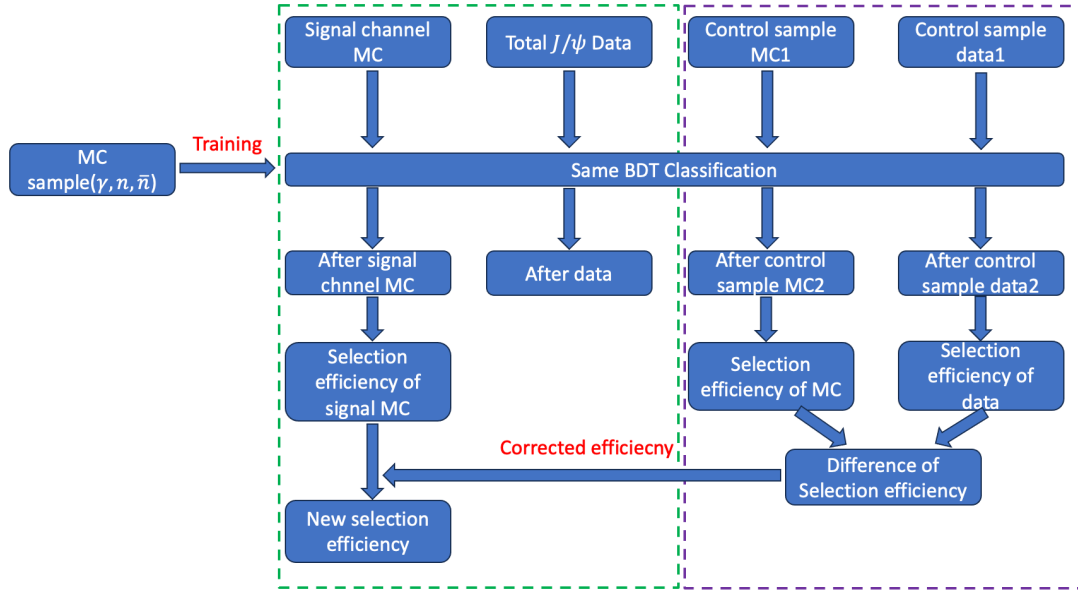
Fig. 15: Correction flow of efficiency

Efficiency corrections are applied following two steps. Firstly, using control samples of two processes $J/\psi \to p\bar{n}\pi^-$ and $J/\psi \to \bar{p}n\pi^+$, the selection efficiencies of MC and data along with different momentum and polar angle bins can be determined. For each bin, the efficiency ratio between data and MC could be calculated by:

$$f_i = \frac{\epsilon_i^{data}}{\epsilon_i^{MC}}, \tag{1}$$

where ϵ_i^{data} is the selection efficiency obtained using data and ϵ_i^{MC} is the selection efficiency obtained using MC, and f_i represents a correction factor. Two dimensional histograms corresponding to efficiency correction factors are shown in Figure 12-14.

Then, the overall selection efficiency obtained using signal MC sample can be corrected in below way:

$$\epsilon_{corr} = \frac{\sum_{i=1}^{N} n_i \times f_i}{N_{truth}}, \tag{2}$$

where n_i represents the number of observed events in i_{th} bin of two dimensional efficiency histogram, N_{truth} denotes the total number of events in signal MC sample, and f_i represents the efficiency correction factor in the i_{th} bin.

5.4 Differential selection efficiency in the $M(n\bar{n})$ frame

The differential selection efficiency in the $M(n\bar{n})$ frame is determined with 20 million signal events generated by a PHSP event generator. Here, the differential efficiency is parameterized with this formula:

$$\epsilon(M) = \frac{\sqrt{(M - 0.939)^2 - 3.53064} \times (3.097 - (M - 0.939)^2)^{2.622}}{118.818 \times (((M - 0.939)^2 - 3.16164)^2 + 0.02696)} + 0.955 \times (1 - 0.4178(M - 0.939) + 0.04974(M - 0.939)^2).$$

(3)

Figure 16 shows that above formula agrees well with the differential efficiency.
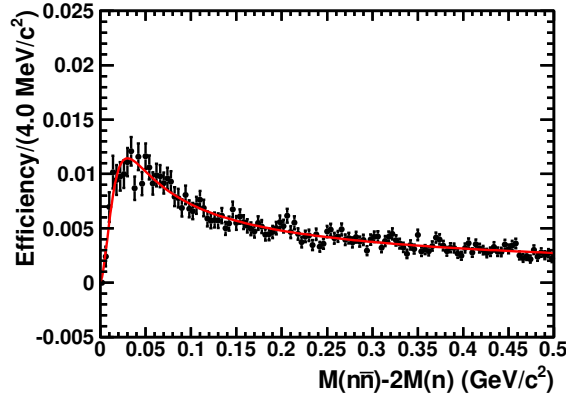
Fig. 16: The efficiency curve of $M(n\bar{n}) - M(n)$ invariant mass for $J/\psi \rightarrow \gamma n\bar{n}$ three body process. The black dots with error bars are MC, and the red solid line is the total fitting function.

5.5 Detector resolution of invariant mass $M(n\bar{n})$

The distribution of the resolution of $M(n\bar{n})$ is determined by $M(n\bar{n})_{\text{rec}} - M(n\bar{n})_{\text{truth}}$. Here, the distribution of the resolution is parameterized with the double gaussian function $DG(M)$, as Figure 17.

Fig. 17: The fitting of invariant mass $M(n\bar{n})$. The black dots with error bars are signal MC by subtracting the truth distribution of $M(n\bar{n})$ from the reconstruction distribution of $M(n\bar{n})$, and the red solid line is the total fitting function.
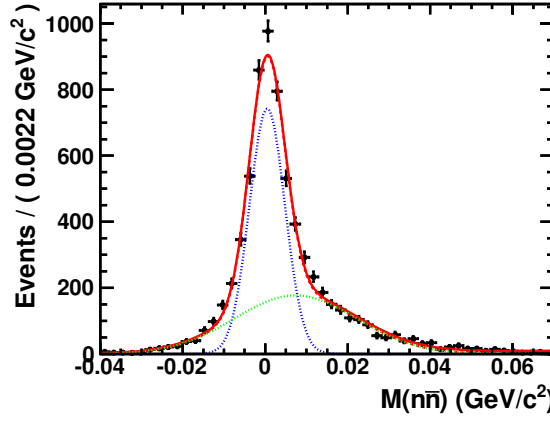
5.6 Results of mass, width, and branching fraction

In the previous analysis, the S-wave Breit-Wigner formula was used to describe the $p\bar{p}$ mass-threshold enhancement [15]. Similarly, the S-wave Breit-Wigner formula can be written as:

$$BW(M) = \left(f \times \frac{q^{2L+1} \times k^3}{\left(M^2 - M_{X(n\bar{n})}^2\right)^2 + M_{X(n\bar{n})}^2 \Gamma_{X(n\bar{n})}^2} \times \epsilon(M) \right) \otimes DG(M), \qquad (4)$$

where $f = 1$ is the FSI factor, q is the momentum of $\bar{n}$ in the rest frames of $n\bar{n}$, k is the momentum of photon in the rest frames of J/ψ, M is the invariant mass of $n\bar{n}$, L is the orbital angular momentum between n and $\bar{n}$ ($L = 0$ for S-wave), $M_{X(n\bar{n})}$ is the mass of $X(n\bar{n})$, $\Gamma_{X(n\bar{n})}$ is the width of $X(n\bar{n})$, $\epsilon(M)$ is the efficiency curve, and $DG(M)$ is the detector resolution.

To yield the signal events, the fitting of the invariant mass of $n\bar{n}$ is performed in the region of [1.879, 2.279] GeV/c^2($M(n\bar{n}) - 2M(n)$ in the region of [0.0, 0.4] GeV/c^2), as shown in Figure 18. The signal is described by the S-wave Breit-Wigner formula. Because the background description of the inclusive MC is not necessarily reliable, the events of three main background channels $J/\psi \to \gamma f_0(2100) \to \gamma n\bar{n}$, $J/\psi \to \gamma f_2(1910) \to \gamma n\bar{n}$, and $J/\psi \to \gamma n\bar{n}$ have been fixed at 1094, 2387, and 1805 by using the proportion components of decay processes $J/\psi \to \gamma f_0(2100) \to \gamma p\bar{p}$, $J/\psi \to \gamma f_2(1910) \to \gamma p\bar{p}$, and $J/\psi \to \gamma p\bar{p}$ according to Ref. [52](page 23). The background shapes of $J/\psi \to \pi^0 n\bar{n}$ and $J/\psi \to \eta n\bar{n}$ are fixed via three-body PHSP model, and the background events of $J/\psi \to \pi^0 n\bar{n}$ and $J/\psi \to \eta n\bar{n}$ are floated and determined through fit. The fitting results, ε_{MC}(selection efficiency) and ε_{corr}(selection efficiency after considering MC efficiency correction) are listed in the Table 7.
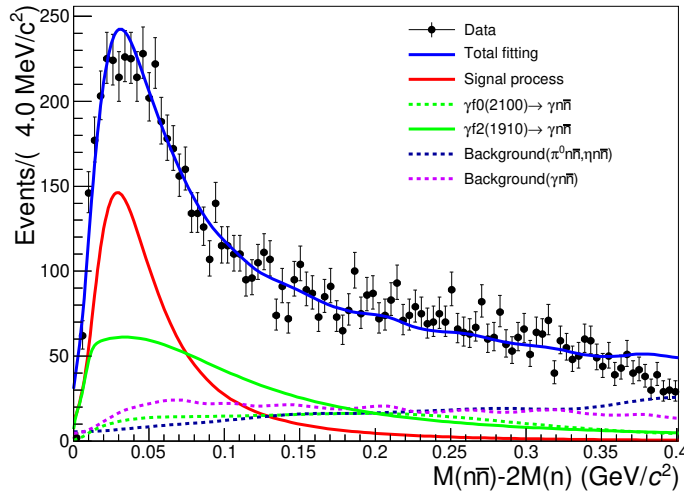
Fig. 18: The distribution of $M(n\bar{n}) - 2M(n)$ for the process J/ψ decay to final states $\gamma n\bar{n}$. The black dots with error bars are the data, the blue solid line is the total fit function, the red line is the signal function, the green line is the background function of $J/\psi \to \gamma f_2(1910) \to \gamma n\bar{n}$ process, the green dashed line is the background function of $J/\psi \to \gamma f_0(2100) \to \gamma n\bar{n}$ process, the purple dashed line is the background function of $J/\psi \to \gamma n\bar{n}$ process, and the blue dashed line is the background function of $J/\psi \to \pi^0 n\bar{n}$ and $J/\psi \to \eta n\bar{n}$ processes.

Tab. 7: The number of signal events, detection efficiency, detection efficiency after considering efficiency correction, mass of $n\bar{n}$, and width of $n\bar{n}$.

Channel	N_{sig}	ε_{MC}	ε_{cor}	Mass (MeV/c^2)	Width (MeV)
$J/\psi \to \gamma X(n\bar{n}) \to n\bar{n}$	2345 ± 89	0.75%	0.437%	1882.6 ± 4.1	58.6 ± 3.7

The branch fraction is calculated according to the formula:

$$
\begin{aligned}
Br(J/\psi \to \gamma X(n\bar{n}) \to \gamma n\bar{n}) &= \frac{N_{sig}}{\varepsilon_{corr} \times N_{tot}} \\
&= \frac{N_{sig}}{\varepsilon_{corr} \times (10087.8 \pm 23.8) \times 10^6} \\
&= \frac{2345 \pm 89}{0.437\% \times (10087.8 \pm 23.8) \times 10^6} = (5.32 \pm 0.20) \times 10^{-5},
\end{aligned}
\tag{5}
$$

where $Br(J/\psi \to \gamma X(n\bar{n}) \to \gamma n\bar{n})$ represents the branching fraction, N_{sig} is the signal events, ε_{corr} is the selection efficiency after considering the difference between data and MC, and N_{tot} is the total number of J/ψ events.

6 Systematic uncertainties

The systematic uncertainties of the branching fraction, mass, and width are studied separately. The uncertainties include efficiency correction, kinematic fitting, the requirement of ΔE, π^0 mass window, fitting method, background estimation, and MC statistics.

6.1 Systematic uncertainties of branching fraction

The total systematic uncertainties of branching fraction are listed in Table 8, and expanded explanations in the following sections.

Tab. 8: The total uncertainties of the branching fraction.

Component	$Br(\%)$
Bin of correction ratio	3.2
Efficiency correction	0.2
Requirement of $\chi^2_{2C}(\gamma n\bar{n}) \leq 15$	5.8
Requirement of $\chi^2_{2C}(\gamma n\bar{n}) \leq \chi^2_{2C}(\gamma\gamma n\bar{n})$	3.1
Requirement of $\chi^2_{2C\ \mathrm{err}}(\gamma n\bar{n})$	6.7
ΔE requirement	1.1
π^0 mass window	2.1
Efficiency curve	8.6
Background estimation	3.8
Fitting range	3.8
Total number $N_{J/\psi}$	0.6
Total uncertainties	12.4

6.1.1 Bin of correction ratio

The correction ratios of two dimensional histograms are shown in Figure 12-14. We have performed linear interpolation in different momentum intervals changing the width of bin from 0.2 GeV to 0.1 GeV. The change of results, 3.2%, is taken as systematic uncertainty.

6.1.2 Efficiency correction

The selection efficiencies of neutrons and anti-neutrons in the EMC detector and BDT method, and the selection efficiency of anti-neutrons in the TOF detector have been studied and corrected using control samples of the processes $J/\psi \rightarrow p\bar{n}\pi^-$ and $J/\psi \rightarrow \bar{p}n\pi^+$. The systematic uncertainties of efficiency correction are estimated using the following formula:

$$\Delta^2 = \sum_{i=0}^{n} \left(\frac{\epsilon_i - \epsilon_0}{\epsilon_0} \right)^2,$$

where n denotes the number of bins of two dimensional histograms, as shown in Figure 12-14, ϵ_0 is the nominal value of corrected efficiency, and the efficiency ϵ_i is obtained after varying the correction factor within 1σ for the i_{th} bin. The value of this systematic uncertainty is about 0.2%.

6.1.3 The requirement of kinematic fitting for $J/\psi \rightarrow \gamma n\bar{n}$

In our analysis, we apply the requirement of $\chi^2_{2C} \leq 15$, then take the measurement of branching fraction under this requirement as nominal values. In order to consider systematic uncertainty from kinematic fitting, we change the value of requirement of $\chi^2_{2C} \leq 15$ from 15 to 10, 15, 20, 25, 30, 35, 40, 45, 50, and compare different results of branching fraction, which are shown in Figure 19 (right panels). In addition, we use the Barlow test method to determine whether the systematic uncertainty of this requirement should be taken into account. As long as there is a Barlow test value greater than 2 in this test, we will consider systematic uncertainty. For example, the Barlow test ξ of the branching fraction is calculated by $\xi = \frac{|Br_{\text{nominal}} - Br_{\text{test}}|}{\sqrt{\sigma^2_{\text{nominal}} - \sigma^2_{\text{test}}}}$, where Br_{test} represents the different branching fractions after applying different requirements of χ^2_{2C}, Br_{nominal} represents nominal branching fraction, and σ_{nominal} and σ_{test} represent their uncertainties. The distributions of Barlow tests of branching fraction are shown in Figure 19 (left panels). For different results, they are described by using the first order polynomial (right panels), and we take the maximum difference between the results of first order polynomial fitting and the nominal value as the systematic uncertainties, as shown in Table 9.

Tab. 9: Systematic uncertainty arising from the kinematic fitting with respect to branching fraction for $J/\psi \rightarrow \gamma X(n\bar{n}) \rightarrow \gamma n\bar{n}$ process.

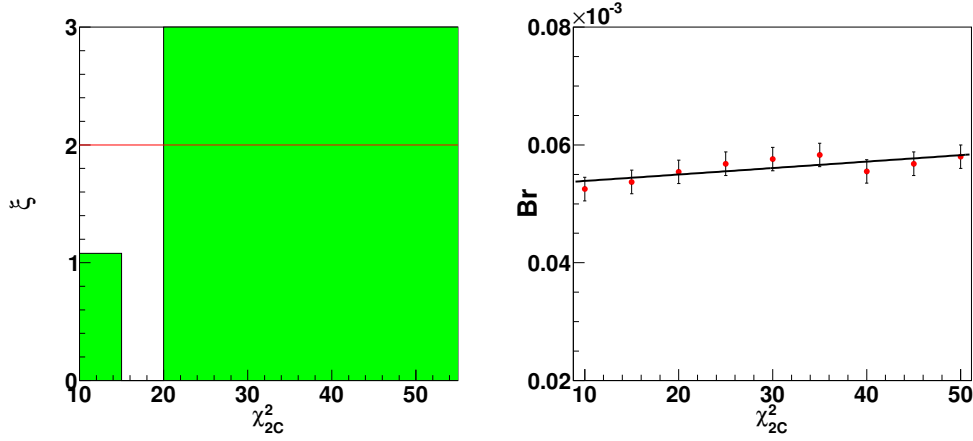| Results	Nominal ($\times 10^{-5}$)	Barlow method ($\times 10^{-5}$)	Difference
$Br(J/\psi \rightarrow \gamma X(n\bar{n}) \rightarrow \gamma n\bar{n})$	5.32 ± 0.20	5.63 ± 0.20	0.31

Fig. 19: (Left) The Barlow test of different χ^2_{2C} requirements for branching fraction. The green histogram represent the values of Barlow test in different requirements. (Right) Red data points and black error bars give different values of branching fraction in different χ^2_{2C} requirements.

6.1.4 The requirement of $\chi^2_{2C}(\gamma n\bar{n}) \leq \chi^2_{2C}(\gamma\gamma n\bar{n})$

The distributions of $\chi^2_{2C}(\gamma\gamma n\bar{n})$ before and after using this requirement $\chi^2_{2C}(\gamma n\bar{n}) \leq \chi^2_{2C}(\gamma\gamma n\bar{n})$ are shown in Figure 20. Here, the $\chi^2_{2C}(\gamma\gamma n\bar{n})$ distributions are consistent between data and MC. Here, we employ a conservative approach to estimate the systematic uncertainty comparing the results with and without this requirement. The difference of the branching fraction is taken as the systematical uncertainty, as shown in Table 10.

Tab. 10: Systematic uncertainty arising from $\chi^2_{2C}(\gamma n\bar{n}) \leq \chi^2_{2C}(\gamma\gamma n\bar{n})$ with respect to branching fraction for $J/\psi \to \gamma X(n\bar{n}) \to \gamma n\bar{n}$ process.

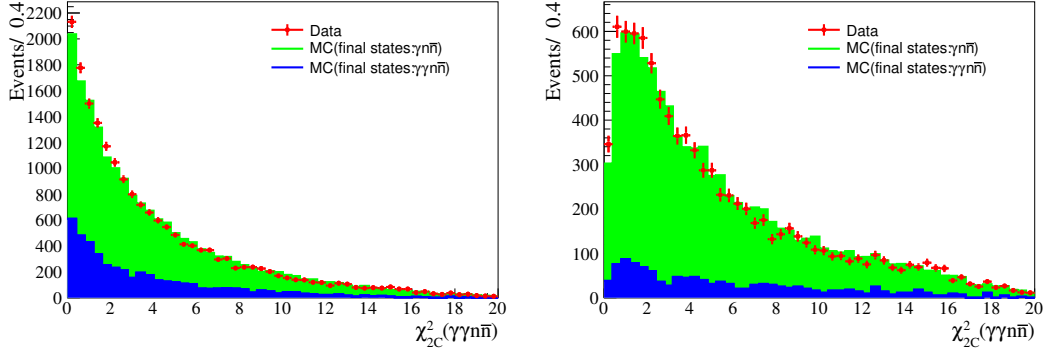| Results	Nominal ($\times 10^{-5}$)	New result ($\times 10^{-5}$)	Difference
$Br(J/\psi \to \gamma X(n\bar{n}) \to \gamma n\bar{n})$	5.32 ± 0.20	5.49 ± 0.16	0.17

Fig. 20: The $\chi^2_{2C}(\gamma\gamma n\bar{n})$ distributions for data, MC (including $J/\psi \rightarrow \gamma n\bar{n}$, $J/\psi \rightarrow \gamma X(n\bar{n}) \rightarrow \gamma n\bar{n}$, $J/\psi \rightarrow \gamma f_0(2100) \rightarrow \gamma n\bar{n}$, and $J/\psi \rightarrow \gamma f_2(1910) \rightarrow \gamma n\bar{n}$, $J/\psi \rightarrow \pi^0 n\bar{n}$, and $J/\psi \rightarrow \eta n\bar{n}$). The red dots with error bars are the data. The blue and green histogram represent $\chi^2_{2C}(\gamma\gamma n\bar{n})$ distributions of the $\gamma n\bar{n}$ and $\gamma\gamma n\bar{n}$ final states, respectively. The left and right figures represent the distribution before and after using this requirement $\chi^2_{2C}(\gamma n\bar{n}) \leq \chi^2_{2C}(\gamma\gamma n\bar{n})$.

6.1.5 The requirement of $\chi^2_{2C\_\mathrm{err}}(\gamma n\bar{n})$

In our analysis, to eliminate error combinations between photon and neutron candidates, we conducted a kinematic fitting of the error combinations and required that the status of kinematic fitting should be unsuccessful. In the kinematic fitting of the error combination, for the photon candidate, photon is assigned neutron mass ($0.93956\ \mathrm{GeV}/c^2$), and for the neutron candidate, neutron is assigned photon mass ($0.0\ \mathrm{GeV}/c^2$). Here, we employ a conservative approach to estimate the systematic uncertainty comparing the results with and without this requirement. The differences in branching fraction is taken as the systematical uncertainties, as shown in Table 11.

Tab. 11: Systematic uncertainty arising from $\chi^2_{2C\_\mathrm{err}}(\gamma n\bar{n})$ with respect to branching fraction for $J/\psi \rightarrow \gamma X(n\bar{n}) \rightarrow \gamma n\bar{n}$ process.

Results	Nominal ($\times 10^{-5}$)	New result ($\times 10^{-5}$)	Difference
$Br(J/\psi \rightarrow \gamma X(n\bar{n}) \rightarrow \gamma n\bar{n})$	5.32 ± 0.20	5.68 ± 0.24	0.36

6.1.6 ΔE requirement

The distribution of the difference of energy between neutron and anti-neutron ΔE is used to remove potential background contributions, such as $J/\psi \rightarrow n\bar{n}$, $J/\psi \rightarrow \gamma\eta'(\eta' \rightarrow \pi^0\pi^0\eta, \eta \rightarrow \gamma\gamma)$, $J/\psi \rightarrow \pi^0 K_L K_S$, and $J/\psi \rightarrow \pi^0\pi^0\gamma$. We applied the requirement of $\Delta E \leq 0.22$ GeV, then took the measurement of branching fraction under this requirement as nominal values. In order to consider systematic uncertainty from ΔE requirement, we changed the value of ΔE requirement from 0.22 to 0.195, 0.200, 0.205, 0.210, 0.215, 0.220, 0.225, 0.230, 0.235, 0.240, and 0.245 GeV/c^2. We compared the results of branching fraction, as shown in Figure 21 (right panels). In addition, we adopted the same

Barlow test method to determine whether the systematic uncertainty of this requirement should be taken into account. The Barlow tests of branching fraction are listed in Figure 21 (left panels). The different results are described using a first order polynomial, and we took the maximum difference between the results of first order polynomial fitting and the nominal value as the systematic uncertainties, as shown in Table 12.

Tab. 12: Systematic uncertainty arising from ΔE with respect to branching fraction for $J/\psi \to \gamma X(n\bar{n}) \to \gamma n\bar{n}$ process.

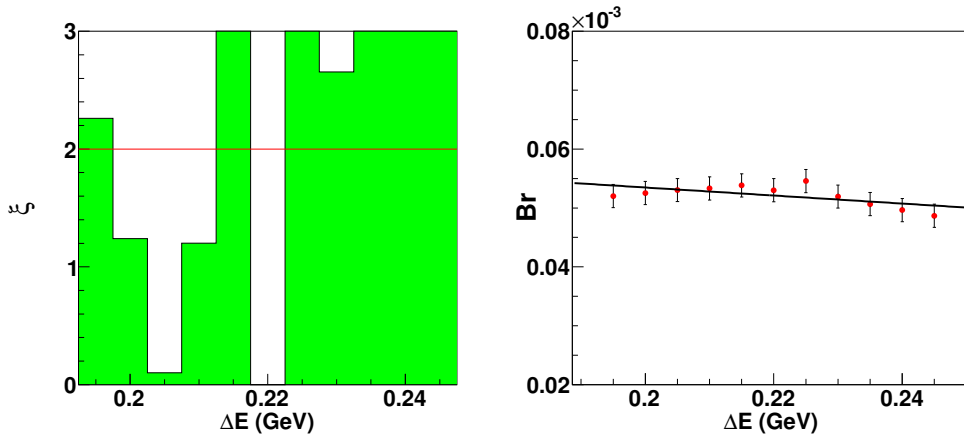| Results	Nominal ($\times 10^{-5}$)	Barlow method ($\times 10^{-5}$)	Difference
$Br(J/\psi \to \gamma X(n\bar{n}) \to \gamma n\bar{n})$	5.32 ± 0.20	5.13 ± 0.20	0.19

Fig. 21: (Left) The Barlow test of different ΔE requirement for branching fraction. The green histogram represent the values of Barlow test in different requirements. (Right) Red data points and black error bars give different values of branching fraction in different ΔE requirements.

6.1.7 π^0 window

In order to remove π^0-related background contributions, such as the $J/\psi \to \pi^0\gamma\gamma$, $J/\psi \to \pi^0 n\bar{n}$, $J/\psi \to \pi^0\pi^0\pi^0\gamma$, $J/\psi \to \pi^0 K_L K_S(K_S \to \pi^0\pi^0)$, and $J/\psi \to \pi^0\pi^0\omega$, and other background contributions of involving π^0 final sate, a π^0 mass window within (0.11, 0.16) is applied. To consider this systematic uncertainty, we change the mass window from (0.11, 0.16) GeV/c^2 to (0.105, 0.16) GeV/c^2, (0.106, 0.16) GeV/c^2, (0.107, 0.16) GeV/c^2, (0.108, 0.16) GeV/c^2, (0.109, 0.16) GeV/c^2, (0.111, 0.16) GeV/c^2, (0.112, 0.16) GeV/c^2, (0.113, 0.16) GeV/c^2, (0.14, 0.16) GeV/c^2, (0.115, 0.16) GeV/c^2 by only varying the lower bound, and compare different results of branching fraction, which are shown in Figure 22 (right panels). We further change the mass window from (0.11, 0.16) GeV/c^2 to (0.11, 0.155) GeV/c^2, (0.11, 0.156) GeV/c^2, (0.11, 0.157) GeV/c^2, (0.11, 0.158) GeV/c^2, (0.11, 0.159) GeV/c^2, (0.11, 0.161) GeV/c^2, (0.11, 0.162) GeV/c^2, (0.11, 0.163) GeV/c^2, (0.11, 0.164) GeV/c^2, (0.11, 0.165) GeV/c^2 by only varying the

436 upper bound, and compare different results of branching fraction, as shown in Figures 23 (right panels).

437 In addition, we adopted the same Barlow test method to determine whether the systematic uncertainty

438 should be considered. The Barlow tests of branching fraction are listed in the following Figure 22 and

439 Figure 23 (left panels). The different results are described using the first order polynomial, and we take

440 the maximum difference between the results of first order polynomial fitting and the nominal value as the

441 systematic uncertainties, as shown in Table 13.

Tab. 13: Systematic uncertainty arising from π^0 mass window with respect to branching fraction for $J/\psi \to \gamma X(n\bar{n}) \to \gamma n\bar{n}$ process.

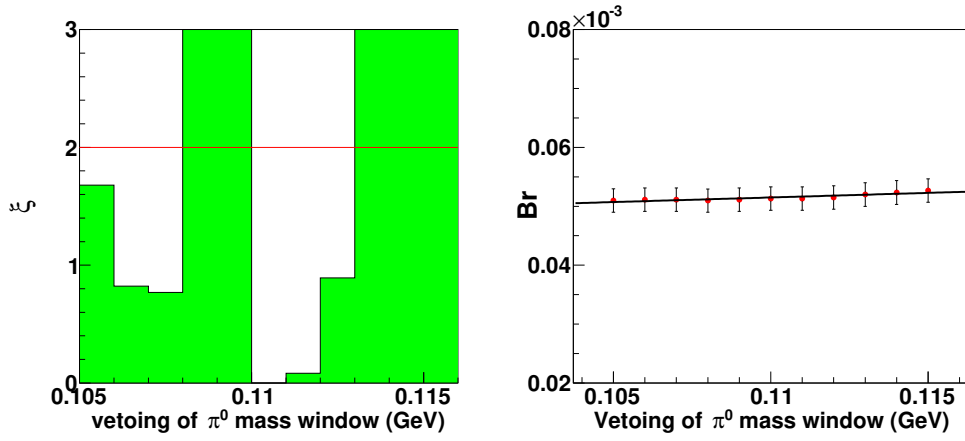| Results	Nominal ($\times 10^{-5}$)	Barlow method ($\times 10^{-5}$)	Difference
$Br(J/\psi \to \gamma X(n\bar{n}) \to \gamma n\bar{n})$	5.32 ± 0.20	5.43 ± 0.24	0.11

Fig. 22: (Left) The Barlow test of different π^0 mass window requirements for branching fraction. The green histogram represent the values of Barlow test in different requirements. (Right) Red data points and black error bars give different values of branching fraction in different π^0 mass window requirements.
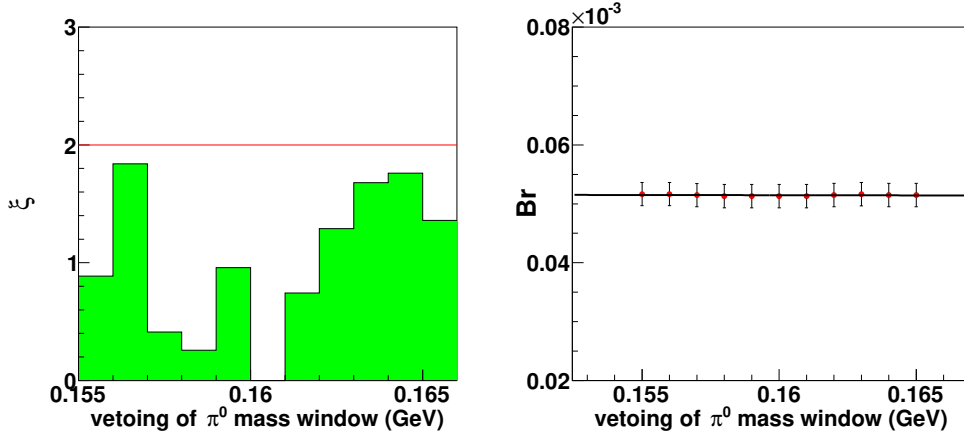
Fig. 23: (Left) The Barlow test of different π^0 mass window requirements for branching fraction. The green histogram represent the values of Barlow test in different requirements. (Right) Red data points and black error bars give different values of branching fraction in different π^0 mass window requirements.

6.1.8 Efficiency curve

In the fitting process, we use the BW formula of S-wave multiplied by the efficiency curve as the shape of the signal. Here, instead of the previous polynomial describing the efficiency curve, we use the new polynomial to describe the efficiency curve, as shown in Figure 24, and use the binned efficiency(Hist PDF) to check the systematic. The results of branching fraction are listed in Table 14, and take the maximum difference between the new results and the nominal value as the uncertainties.

Tab. 14: Systematic uncertainty arising from the fitting method with respect to branching fraction for $J/\psi \rightarrow \gamma X(n\bar{n}) \rightarrow \gamma n\bar{n}$ process.

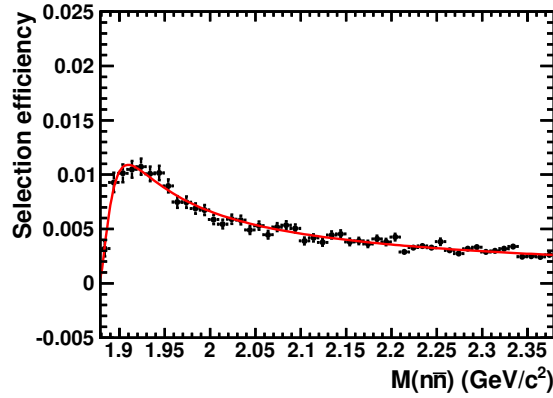| Results	Nominal ($\times 10^{-5}$)	New efficiency curve ($\times 10^{-5}$)	Difference
$Br(J/\psi \rightarrow \gamma X(n\bar{n}) \rightarrow \gamma n\bar{n})$	5.32 ± 0.20	4.86 ± 0.20	0.46

Fig. 24: The efficiency curve for $J/\psi \rightarrow \gamma n\bar{n}$ three body process. The black dots with error bars are the data, and the red solid line is the total fitting function.

6.1.9 Background estimation

To estimate the uncertainties of background events and shapes of $J/\psi \rightarrow \gamma f_0(2100) \rightarrow \gamma n\bar{n}$, $J/\psi \rightarrow \gamma f_2(1910) \rightarrow \gamma n\bar{n}$, and $J/\psi \rightarrow \gamma n\bar{n}$, we considered the new proportion components of $J/\psi \rightarrow \gamma f_0(2100) \rightarrow \gamma n\bar{n}$, $J/\psi \rightarrow \gamma f_2(1910) \rightarrow \gamma n\bar{n}$, and $J/\psi \rightarrow \gamma n\bar{n}$ in our fitting method, and the proportion of each component differ from nominal fitting method, as shown in Figure 25. In previous analysis, the proportion components of $J/\psi \rightarrow \gamma f_0(2100) \rightarrow \gamma p\bar{p}$, $J/\psi \rightarrow \gamma f_2(1910) \rightarrow \gamma p\bar{p}$ are obtained from another PWA result according to Ref. [52] (page 11). Therefore, the events of three main background channels $J/\psi \rightarrow \gamma f_0(2100) \rightarrow \gamma n\bar{n}$, $J/\psi \rightarrow \gamma f_2(1910) \rightarrow \gamma n\bar{n}$, and $J/\psi \rightarrow \gamma n\bar{n}$ are fixed to be 1094, 2387, and 1805 based on the decay channels of $J/\psi \rightarrow \gamma f_0(2100) \rightarrow \gamma p\bar{p}$, $J/\psi \rightarrow \gamma f_2(1910) \rightarrow \gamma p\bar{p}$, and $J/\psi \rightarrow \gamma p\bar{p}$ [52](page 11). The background shapes of $J/\psi \rightarrow \pi^0 n\bar{n}$ and $J/\psi \rightarrow \eta n\bar{n}$ are fixed via three-body PHSP model, and background events of $J/\psi \rightarrow \pi^0 n\bar{n}$ and $J/\psi \rightarrow \eta n\bar{n}$ are floated and determined through the fitting. Comparing the nominal values, the difference of the result of branching fraction is taken as the systematic uncertainties, as shown in Table 15.

Tab. 15: Systematic uncertainty arising from the background estimation with respect to branching fraction, mass of $n\bar{n}$, and width of $n\bar{n}$ for $J/\psi \rightarrow \gamma X(n\bar{n}) \rightarrow \gamma n\bar{n}$ process.

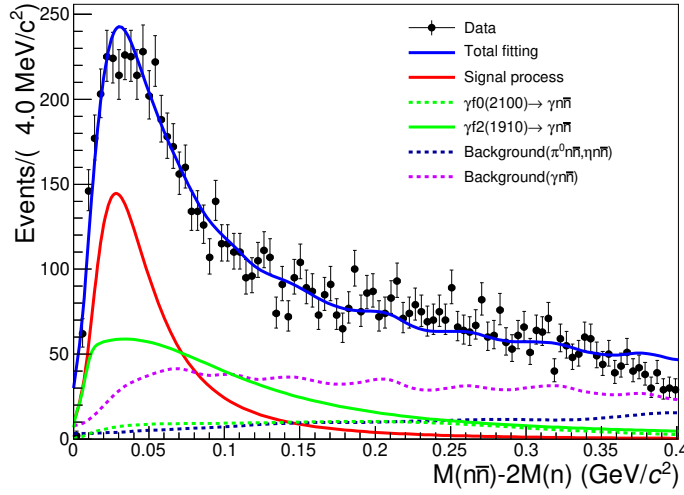| Results	Nominal ($\times 10^{-5}$)	Barlow method ($\times 10^{-5}$)	Difference
$Br(J/\psi \rightarrow \gamma X(n\bar{n}) \rightarrow \gamma n\bar{n})$	5.32 ± 0.20	5.02 ± 0.21	0.20

Fig. 25: The distribution of $M(n\bar{n}) - 2M(n)$ for the process J/ψ decay to final states $\gamma n\bar{n}$. The black dots with error bars are the data, the blue solid line is the total fitting function, the red line is the signal function, the green line is the background function of $J/\psi \rightarrow \gamma f_2(1910) \rightarrow \gamma n\bar{n}$ process, the green dashed line is the background function of $J/\psi \rightarrow \gamma f_0(2100) \rightarrow \gamma n\bar{n}$ process, the purple dashed line is the background function of $J/\psi \rightarrow \gamma n\bar{n}$ process, and the blue dashed line is the background function of $J/\psi \rightarrow \pi^0 n\bar{n}$ and $J/\psi \rightarrow \eta n\bar{n}$ processes.

6.1.10 Fitting range

To estimate the uncertainties of the fitting range, changing from [0.0, 0.4] to [0.0, 0.35] GeV/c^2, the fitting results are listed in the following Table 16, and take the difference with the nominal values as the uncertainties.

Tab. 16: Systematic uncertainty arising from the fitting range with respect to branching fraction, mass of $n\bar{n}$, and width of $n\bar{n}$ for $J/\psi \rightarrow \gamma X(n\bar{n}) \rightarrow \gamma n\bar{n}$ process.

Results	Nominal ($\times 10^{-5}$)	new range ($\times 10^{-5}$)	Difference
$Br(J/\psi \rightarrow \gamma X(n\bar{n}) \rightarrow \gamma n\bar{n})$	5.32 ± 0.20	5.02 ± 0.20	0.20

6.1.11 Total number of J/ψ

The number of J/ψ is related to the measurement of branch fraction, so we need to consider the uncertainty of the number of J/ψ. The total number of J/ψ events are obtained based on inclusive hadronic events, as described in [54]. The uncertainty of the total number is determined to be 0.4% for J/ψ events.

6.2 Systematic uncertainties of mass and width

The total systematic uncertainties of the mass and width are listed in Table 17, and expanded explanations in the following sections.

Tab. 17: The total uncertainties of the mass and width of $n\bar{n}$.

Component	Mass	Width
Efficiency correction	0.9	4.4
Requirement of $\chi^2_{2C}(\gamma n\bar{n}) \leq 15$	2.3	2.6
Requirement of $\chi^2_{2C}(\gamma n\bar{n}) \leq \chi^2_{2C}(\gamma\gamma n\bar{n})$	4.2	6.0
Requirement of $\chi^2_{2C\ \text{err}}(\gamma n\bar{n})$	2.2	6.1
ΔE requirement	–	0.3
π^0 mass window	1.1	1.1
Fitting method(efficiency curve)	19.1	14.8
Background estimation	0.8	4.7
Fitting range	6.7	3.3
Total uncertainties	21.0	18.8

6.2.1 Efficiency correction

Using Breit-Wigner formula, the mass and width of $X(n\bar{n})$ can be obtained by fitting invariant mass of $n\bar{n}$. Here, the efficiency curve has been considered in Breit-Wigner formula. In order to study the uncertainty of the efficiency curve, we correct selection efficiency in each bin of $M(n\bar{n})$ from 1.878 to 2.379 GeV/c^2. The correction method is based on Eq. 2 in Section 5.3. In Figure 26, the left figure indicates that the efficiency correction has not been considered, while the right figure indicates that the efficiency correction has been considered. Although we found that the difference of the value of selection efficiency is quite large between left figure and right figure, the difference between these two efficiency curves' shapes is very small. Therefore, we could apply the two efficiency curves in Breit-Wigner formula, then calculate the differences in branching fraction, mass, and width before and after correction as the systematic uncertainties, as listed in Table 18.
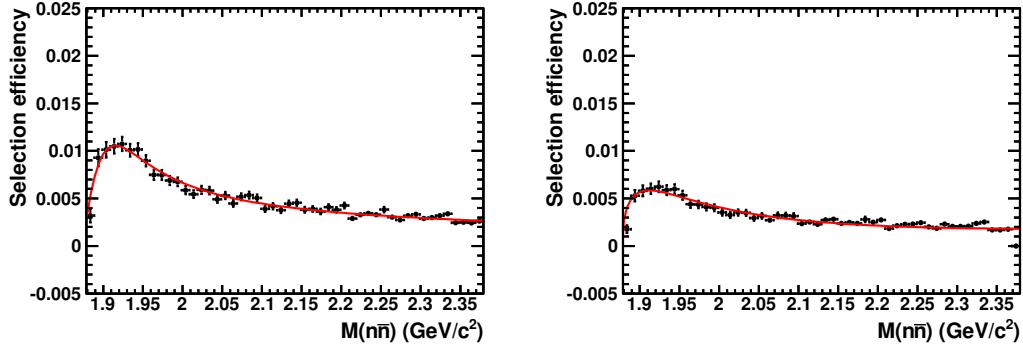
Fig. 26: The efficiency curve of $n\bar{n}$ invariant mass for $J/\psi \rightarrow \gamma n\bar{n}$ three body process. The black dots with error bars are the data, and the red solid line is the total fitting function. The left figure indicates that efficiency correction has not been considered, while the right figure indicates that the efficiency correction has been considered.

Tab. 18: Systematic uncertainty arising from the efficiency correction with respect to the mass and the width of $n\bar{n}$ for $J/\psi \rightarrow \gamma X(n\bar{n}) \rightarrow \gamma n\bar{n}$ process.

Results	Nominal	With efficiency correction	Difference
$M_{X(n\bar{n})}$ (MeV/c^2)	1882.6 ± 4.1	1883.5 ± 3.7	0.9
$\Gamma_{X(n\bar{n})}$ (MeV)	58.6 ± 3.7	54.2 ± 3.3	4.4

6.2.2 The requirement of kinematic fitting for $J/\psi \rightarrow \gamma n\bar{n}$

In our analysis, we apply the requirement of $\chi^2_{2C} \leq 15$, then take the measurements of mass and width under this requirement as nominal values. In order to consider systematic uncertainty from kinematic fitting, we change the value of requirement of $\chi^2_{2C} \leq 15$ from 15 to 10, 15, 20, 25, 30, 35, 40, 45, and 50, and compare different results of mass and width, which are shown in Figure 27, and Figure 28 (right panels). The distributions of Barlow tests of mass and width are shown in Figure 27 and Figure 28 (left panels). For different results, they are described by using the first order polynomial (right panels), and we take the maximum difference between the results of first order polynomial fitting and the nominal value as the systematic uncertainties, as shown in Table 19.

Tab. 19: Systematic uncertainty arising from the kinematic fitting with respect to mass of $n\bar{n}$ and width of $n\bar{n}$ for $J/\psi \rightarrow \gamma X(n\bar{n}) \rightarrow \gamma n\bar{n}$ process.

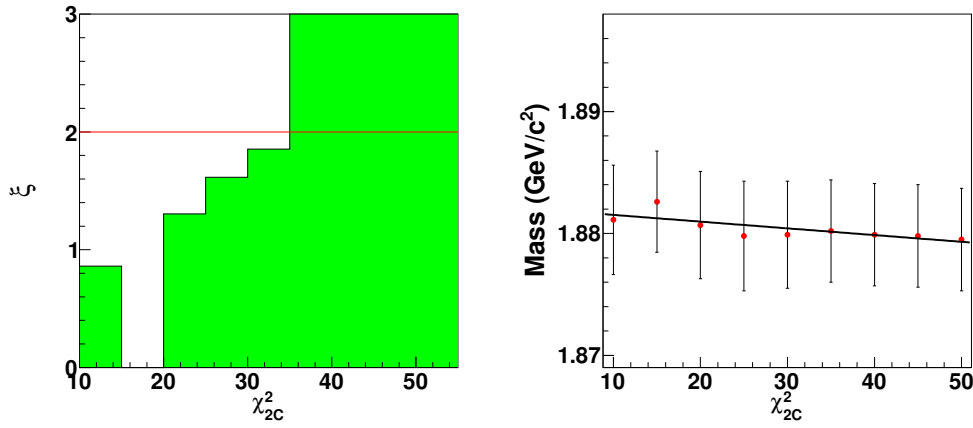| Results	Nominal	Barlow method	Difference
$M_{X(n\bar{n})}$ (MeV/c^2)	1882.6 ± 4.1	1880.3 ± 4.1	2.3
$\Gamma_{X(n\bar{n})}$ (MeV)	58.6 ± 3.7	61.2 ± 3.7	2.6

Fig. 27: (Left) The Barlow test of different χ^2_{2C} requirements for mass. The green histogram represent the values of Barlow test in different requirements. (Right) Red data points and black error bars give different values of mass in different χ^2_{2C} requirements.
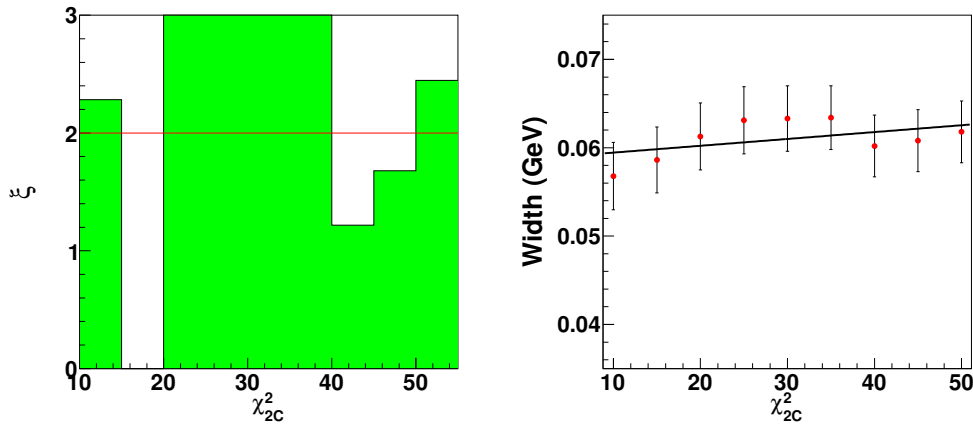

Fig. 28: (Left) The Barlow test of different χ^2_{2C} requirements for width. The green histogram represent the values of Barlow test in different requirements. (Right) Red data points and black error bars give different values of width in different χ^2_{2C} requirements.

6.2.3 The requirement of $\chi^2_{2C}(\gamma n\bar{n}) \le \chi^2_{2C}(\gamma\gamma n\bar{n})$

The distributions of $\chi^2_{2C}(\gamma\gamma n\bar{n})$ before and after using this requirement $\chi^2_{2C}(\gamma n\bar{n}) \le \chi^2_{2C}(\gamma\gamma n\bar{n})$ are shown in Figure 20. Here, the $\chi^2_{2C}(\gamma\gamma n\bar{n})$ distributions are consistent between data and MC. Here, we employ a conservative approach to estimate the systematic uncertainty comparing the results with and without this requirement. The differences in mass and width are taken as the systematical uncertainties, as shown in Table 20.

Tab. 20: Systematic uncertainty arising from $\chi^2_{2C}(\gamma n\bar{n}) \leq \chi^2_{2C}(\gamma\gamma n\bar{n})$ with respect to mass and width of $n\bar{n}$ for $J/\psi \to \gamma X(n\bar{n}) \to \gamma n\bar{n}$ process.

Results	Nominal	Barlow method	Difference
$M_{X(n\bar{n})}$ (MeV/c^2)	1882.6 ± 4.1	1886.8 ± 2.3	4.2
$\Gamma_{X(n\bar{n})}$ (MeV)	58.6 ± 3.7	52.6 ± 2.7	6.0

6.2.4 The requirement of $\chi^2_{2C\_err}(\gamma n\bar{n})$

In our analysis, to eliminate error combinations between photon and neutron candidates, we conducted a kinematic fitting of the error combinations and required that the status of kinematic fitting should be unsuccessful. In the kinematic fitting of the error combination, for the photon candidate, photon is assigned neutron mass (0.93956 GeV/c^2), and for the neutron candidate, neutron is assigned photon mass (0.0 GeV/c^2). Here, we employ a conservative approach to estimate the systematic uncertainty comparing the results with and without this requirement. The differences in mass and width are taken as the systematical uncertainties, as shown in Table 21.

Tab. 21: Systematic uncertainty arising from $\chi^2_{2C\_err}(\gamma n\bar{n})$ with respect to mass and width of $n\bar{n}$ for $J/\psi \to \gamma X(n\bar{n}) \to \gamma n\bar{n}$ process.

Results	Nominal	Barlow method	Difference
$M_{X(n\bar{n})}$ (MeV/c^2)	1882.6 ± 4.1	1880.4 ± 2.4	2.2
$\Gamma_{X(n\bar{n})}$ (MeV)	58.6 ± 3.7	52.5 ± 3.2	6.1

6.2.5 ΔE requirement

We applied the requirement of $\Delta E \leq 0.22$ GeV, then took the measurements of mass and width under this requirement as nominal values. In order to consider systematic uncertainty from ΔE requirement, we changed the value of ΔE requirement from 0.22 to 0.195, 0.200, 0.205, 0.210, 0.215, 0.220, 0.225, 0.230, 0.235, 0.240, and 0.245 GeV/c^2. We compared the results of mass and width, as shown in Figure 29 and Figure 30 (right panels). The Barlow tests of mass and width are listed in Figure 29 and Figure 30 (left panels). The different results are described using a first order polynomial, and we took the maximum difference between the results of first order polynomial fitting and the nominal value as the systematic uncertainties, as shown in Table 22.

Tab. 22: Systematic uncertainty arising from ΔE with respect to mass and width of $n\bar{n}$ for $J/\psi \to \gamma X(n\bar{n}) \to \gamma n\bar{n}$ process.

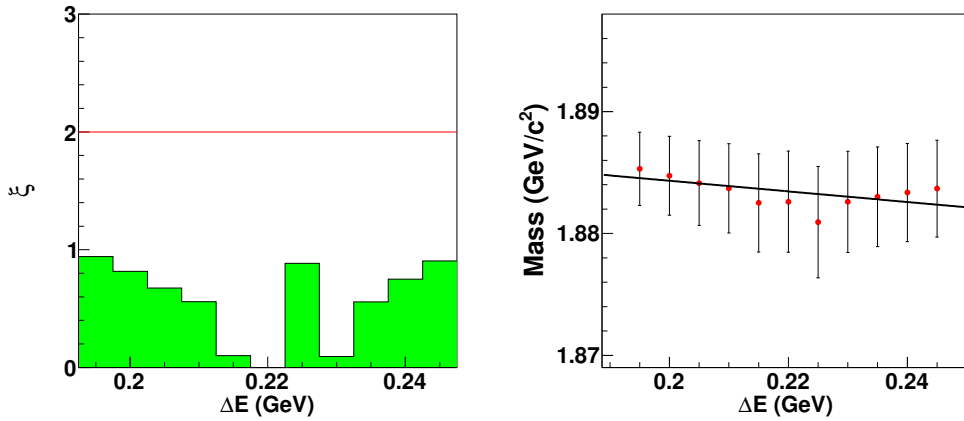| Results	Nominal	Barlow method	Difference
$M_{X(n\bar{n})}$ (MeV/c^2)	1882.6 ± 4.1	–	–
$\Gamma_{X(n\bar{n})}$ (MeV)	58.6 ± 3.7	58.3 ± 4.1	0.3

Fig. 29: (Left) The Barlow test of different ΔE requirements for mass. The green histogram represent the values of Barlow test in different requirements. (Right) Red data points and black error bars give different values of mass in different ΔE requirements.
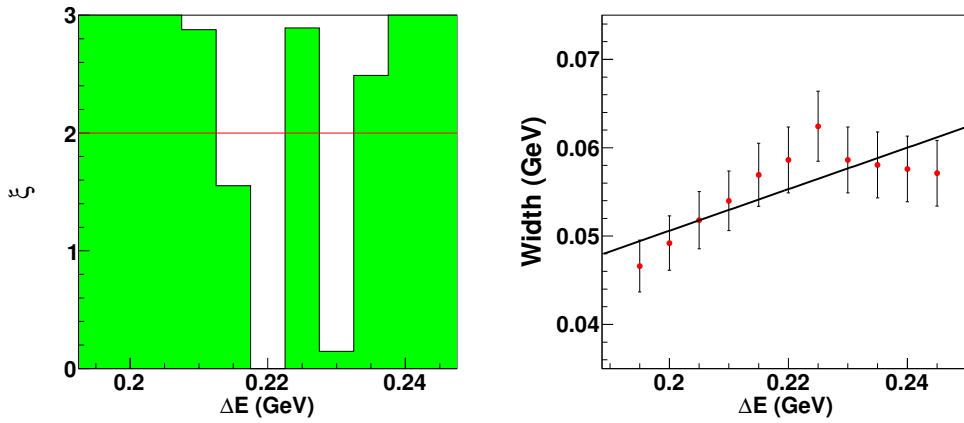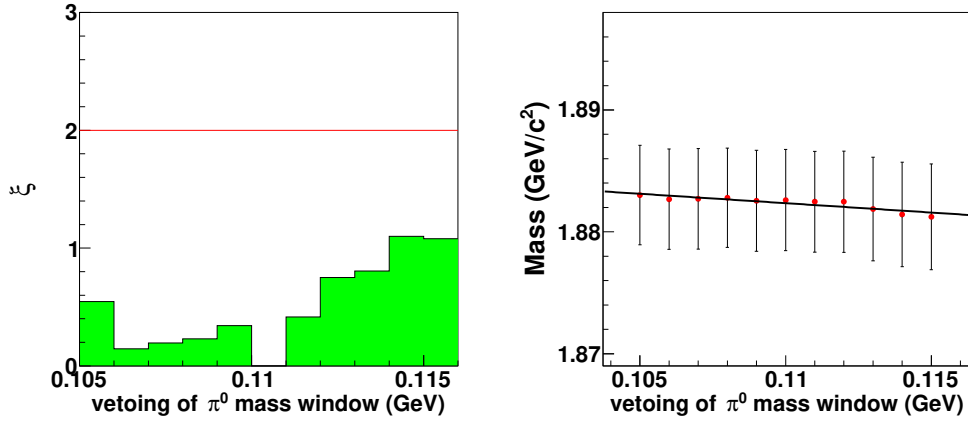

Fig. 30: (Left) The Barlow test of different ΔE requirements for width. The green histogram represent the values of Barlow test in different requirements. (Right) Red data points and black error bars give different values of width in different ΔE requirements.

6.2.6 π^0 window

In order to remove π^0-related background contributions, a π^0 mass window within (0.11, 0.16) is applied. To consider this systematic uncertainty, we change the mass window from (0.11, 0.16) GeV/c^2 to (0.105, 0.16) GeV/c^2, (0.106, 0.16) GeV/c^2, (0.107, 0.16) GeV/c^2, (0.108, 0.16) GeV/c^2, (0.109, 0.16) GeV/c^2, (0.111, 0.16) GeV/c^2, (0.112, 0.16) GeV/c^2, (0.113, 0.16) GeV/c^2, (0.14, 0.16) GeV/c^2, (0.115, 0.16) GeV/c^2 by only varying the lower bound, and compare different results of mass and width, which are shown in Figure 31 and Figure 32 (right panels). We further change the mass window from (0.11, 0.16) GeV/c^2 to (0.11, 0.155) GeV/c^2, (0.11, 0.156) GeV/c^2, (0.11, 0.157) GeV/c^2, (0.11, 0.158) GeV/c^2,

(0.11, 0.159) GeV/c^2, (0.11, 0.161) GeV/c^2, (0.11, 0.162) GeV/c^2, (0.11, 0.163) GeV/c^2, (0.11, 0.164) GeV/c^2, (0.11, 0.165) GeV/c^2 by only varying the upper bound, and compare different results of mass and width, as shown in Figures 33 and Figures 34 (right panels). The Barlow tests of mass and width are listed in the following Figures 31-34 (left panels). The different results are described using the first order polynomial, and we take the maximum difference between the results of first order polynomial fitting and the nominal value as the systematic uncertainties, as shown in Table 23.

Tab. 23: Systematic uncertainty arising from π^0 mass window with respect to mass of and width of $n\bar{n}$ for $J/\psi \to \gamma X(n\bar{n}) \to \gamma n\bar{n}$ process.

Results	Nominal	Barlow method	Difference
$M_{X(n\bar{n})}$ (MeV/c^2)	1882.6 ± 4.1	1881.5 ± 4.1	1.1
$\Gamma_{X(n\bar{n})}$ (MeV)	58.6 ± 3.7	59.7 ± 3.7	1.1

Fig. 31: (Left) The Barlow test of different π^0 mass window requirements for mass. The green histogram represent the values of Barlow test in different requirements. (Right) Red data points and black error bars give different values of mass in different π^0 mass window requirements.
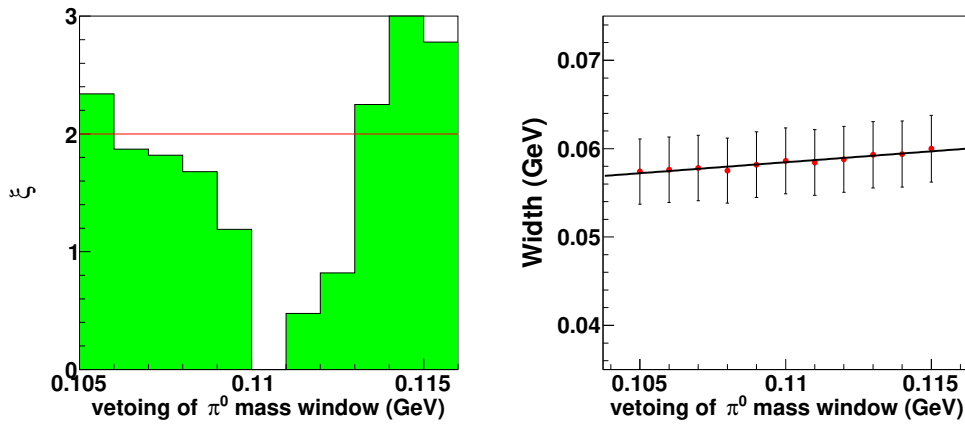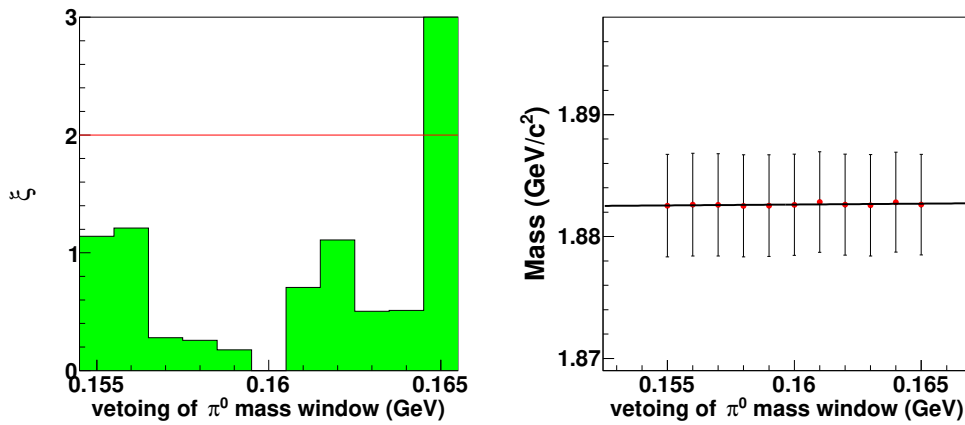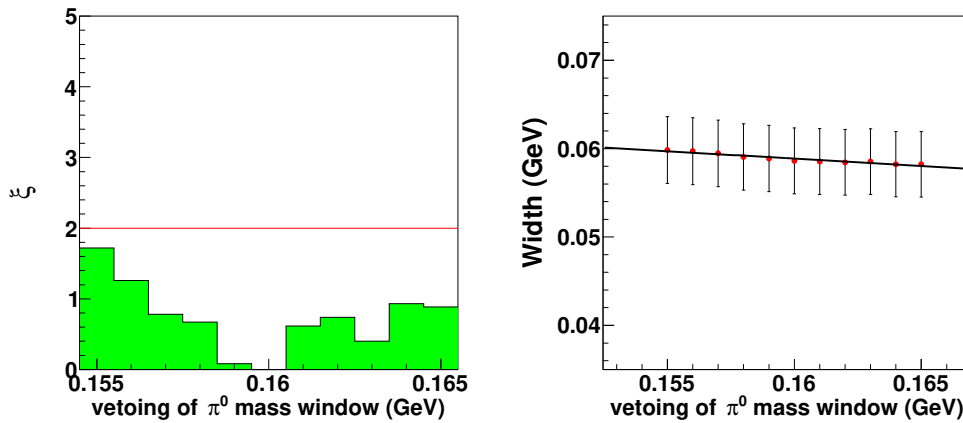
Fig. 32: (Left) The Barlow test of different π^0 mass window requirements for width. The green histogram represent the values of Barlow test in different requirements. (Right) Red data points and black error bars give different values of width in different π^0 mass window requirements.

Fig. 33: (Left) The Barlow test of different π^0 mass window requirements for mass. The green histogram represent the values of Barlow test in different requirements. (Right) Red data points and black error bars give different values of mass in different π^0 mass window requirements.

Fig. 34: (Left) The Barlow test of different π^0 mass window requirements for width. The green histogram represent the values of Barlow test in different requirements. (Right) Red data points and black error bars give different values of width in different π^0 mass window requirements.

6.2.7 Efficiency curve

In the fitting process, we use the BW formula of S-wave multiplied by the efficiency curve as the shape of the signal. Here, instead of the previous polynomial describing the efficiency curve, we use the new polynomial to describe the efficiency curve, as shown in Figure 24, and use the binned efficiency(Hist PDF) to check the systematic. The results of mass and width are listed in Table 24, and take the difference between the new results and the nominal values as the uncertainties.

Tab. 24: Systematic uncertainty arising from the fitting method with respect to branching fraction, mass of $n\bar{n}$, and width of $n\bar{n}$ for $J/\psi \to \gamma X(n\bar{n}) \to \gamma n\bar{n}$ process.

Results	Nominal	New efficiency curve	Difference
$M_{X(n\bar{n})}$ (MeV/c^2)	1882.6 ± 4.1	1901.7 ± 3.5	19.1
$\Gamma_{X(n\bar{n})}$ (MeV)	58.6 ± 3.7	43.8 ± 2.6	14.8

6.2.8 Background estimation

To estimate the uncertainties of background events and shapes of $J/\psi \to \gamma f_0(2100) \to \gamma n\bar{n}$, $J/\psi \to \gamma f_2(1910) \to \gamma n\bar{n}$, and $J/\psi \to \gamma n\bar{n}$, we considered the new proportion components of $J/\psi \to \gamma f_0(2100) \to \gamma n\bar{n}$, $J/\psi \to \gamma f_2(1910) \to \gamma n\bar{n}$, and $J/\psi \to \gamma n\bar{n}$ in our fitting method, and the proportion of each component differ from nominal fitting method, as shown in Figure 25. In previous analysis, the proportion components of $J/\psi \to \gamma f_0(2100) \to \gamma p\bar{p}$, $J/\psi \to \gamma f_2(1910) \to \gamma p\bar{p}$ are obtained from another PWA result according to Ref. [52] (page 11). Therefore, the events of three main background channels $J/\psi \to \gamma f_0(2100) \to \gamma n\bar{n}$, $J/\psi \to \gamma f_2(1910) \to \gamma n\bar{n}$, and $J/\psi \to \gamma n\bar{n}$ are fixed to be 1094, 2387, and 1805 based on the decay channels of $J/\psi \to \gamma f_0(2100) \to \gamma p\bar{p}$, $J/\psi \to \gamma f_2(1910) \to \gamma p\bar{p}$, and

545 $J/\psi \to \gamma p\bar{p}$ [52](page 11). The background shapes of $J/\psi \to \pi^0 n\bar{n}$ and $J/\psi \to \eta n\bar{n}$ are fixed via three-

546 body PHSP model, and background events of $J/\psi \to \pi^0 n\bar{n}$ and $J/\psi \to \eta n\bar{n}$ are floated and determined

547 through the fitting. Comparing the nominal values, the differences of the results of mass and width are

548 taken as the systematic uncertainties, as shown in Table 25.

Tab. 25: Systematic uncertainty arising from the background estimation with respect to mass and width of $n\bar{n}$ for $J/\psi \to \gamma X(n\bar{n}) \to \gamma n\bar{n}$ process.

Results	Nominal	Barlow method	Difference
$M_{X(n\bar{n})}$ (MeV/c^2)	1882.6 ± 4.1	1883.4 ± 3.8	0.8
$\Gamma_{X(n\bar{n})}$ (MeV)	58.6 ± 3.7	53.9 ± 3.5	4.7

549 ### 6.2.9 Fitting range

550 To estimate the uncertainties of the fitting range, changing from [0.0, 0.4] to [0.0, 0.35] GeV/c^2, the

551 fitting results are listed in the following Table 26, and take the difference with the nominal values as the

552 uncertainties.

Tab. 26: Systematic uncertainty arising from fitting range with respect to mass and width of $n\bar{n}$ for $J/\psi \to \gamma X(n\bar{n}) \to \gamma n\bar{n}$ process.

Results	Nominal	New range	Difference
$M_{X(n\bar{n})}$ (MeV/c^2)	1882.6 ± 4.1	1889.3 ± 3.0	6.7
$\Gamma_{X(n\bar{n})}$ (MeV)	58.6 ± 3.7	55.3 ± 3.7	3.3

7   Summary

In summary, based on the 10087×10^6 J/ψ events collected at BESIII detector, the branching fraction of $J/\psi \rightarrow \gamma X(n\bar{n}) \rightarrow \gamma n\bar{n}$ is measured to be $(5.32 \pm 0.20 \pm 0.68) \times 10^{-5}$ for the first time. Table 27 and Table 28 summarize the results of branching fraction, mass, and width. The ratio of $\frac{Br(J/\psi \rightarrow \gamma X(n\bar{n}) \rightarrow \gamma n\bar{n})}{Br(J/\psi \rightarrow \gamma X(p\bar{p}) \rightarrow \gamma p\bar{p})}$ and the difference of $\Delta(M_{X(n\bar{n})} - M_{X(p\bar{p})})$ are calculated to be $0.59^{+0.03}_{-0.08}(stat.)^{+0.13}_{-0.34}(syst.)$ and $50.6^{+6.5}_{-19.4}(stat.)^{+27.7}_{-27.0}(syst.)$ MeV/c^2. Besides, the $M_{X(n\bar{n})}$ and $\Gamma_{X(n\bar{n})}$ are measured to be $1882.6 \pm 4.1 \pm 21.0$ MeV and $58.6 \pm 3.7 \pm 18.8$ MeV, which are consistent with the measurements of $J/\psi \rightarrow \gamma X(p\bar{p}) \rightarrow \gamma p\bar{p}$ within $1.1\ \sigma$. However, all widths of $\Gamma_{X(n\bar{n})}$ and $\Gamma_{X(p\bar{p})}$ are less than widths of $X(1835)$, which may indicate that $X(n\bar{n})$, $X(p\bar{p})$, and $X(1835)$ are potentially mixing. The measurements of branching fraction, mass, and width of $X(n\bar{n})$ can also provide important input for theoretical research and understand the properties of non-perturbative quantum chromodynamics.

Tab. 27: The branching fraction of $J/\psi \rightarrow \gamma X(p\bar{p}) \rightarrow \gamma n\bar{n}$ process

Decay mode	Branching fraction($\times 10^{-4}$)
$J/\psi \rightarrow \gamma X(n\bar{n}) \rightarrow \gamma n\bar{n}$ (Our measurement)	$0.532 \pm 0.020 \pm 0.068$
$J/\psi \rightarrow \gamma X(n\bar{n}) \rightarrow \gamma n\bar{n}$ (Yan liang's work)	0.94 ± 0.21 [57]
$J/\psi \rightarrow \gamma X(p\bar{p}) \rightarrow \gamma p\bar{p}$ (PDG)	$0.90^{+0.04+0.27}_{-0.11-0.55}$ [18]

Tab. 28: The mass and width of $n\bar{n}$, $p\bar{p}$ and $X(1835)$.

Decay mode	Mass(MeV)	Width(MeV)
$X(n\bar{n})$	$1882.6 \pm 4.1 \pm 21.0$	$58.6 \pm 3.7 \pm 18.8$
$X(n\bar{n})$(Yan liang's work)	1897 ± 6	40.8 ± 14.2 [57]
$X(p\bar{p})$	1861^{+6+7}_{-13-26}	<38 at the 90% C.L. [16]
$X(p\bar{p})$	$1832^{+19+18}_{-5-17} \pm 19$	<76 at the 90% C.L. [18]
$X(1835)$	$1826^{+13.0}_{-3.4}$	$242^{+14.0}_{-15}$ [55]

References

[1] M. Gell-Mann, Phys. Lett. **8**, 214-215 (1964) doi:10.1016/S0031-9163(64)92001-3

[2] C. Amsler and N. A. Tornqvist, Phys. Rept. **389**, 61-117 (2004) doi:10.1016/j.physrep.2003.09.003

[3] E. Klempt and A. Zaitsev, Phys. Rept. **454**, 1-202 (2007) doi:10.1016/j.physrep.2007.07.006 [arXiv:0708.4016 [hep-ph]].

[4] J. P. Lees *et al.* [BaBar], Phys. Rev. D **89** (2014) no.11, 111103 doi:10.1103/PhysRevD.89.111103 [arXiv:1211.6271 [hep-ex]].

[5] B. Aubert *et al.* [BaBar], Phys. Rev. D **77** (2008), 111101 doi:10.1103/PhysRevD.77.111101 [arXiv:0803.2838 [hep-ex]].

[6] X. L. Wang *et al.* [Belle], Phys. Rev. Lett. **99** (2007), 142002 doi:10.1103/PhysRevLett.99.142002 [arXiv:0707.3699 [hep-ex]].

[7] S. Jia *et al.* [Belle], Phys. Rev. D **100** (2019) no.11, 111103 doi:10.1103/PhysRevD.100.111103 [arXiv:1911.00671 [hep-ex]].

[8] M. Ablikim *et al.* [BESIII], Phys. Rev. Lett. **118** (2017) no.9, 092002 doi:10.1103/PhysRevLett.118.092002 [arXiv:1610.07044 [hep-ex]].

[9] M. Ablikim *et al.* [BESIII], Phys. Rev. Lett. **129** (2022) no.10, 102003 doi:10.1103/PhysRevLett.129.102003 [arXiv:2203.05815 [hep-ex]].

[10] R. Aaij *et al.* [LHCb], Phys. Rev. Lett. **115** (2015), 072001 doi:10.1103/PhysRevLett.115.072001 [arXiv:1507.03414 [hep-ex]].

[11] R. Aaij *et al.* [LHCb], Phys. Rev. Lett. **122** (2019) no.22, 222001 doi:10.1103/PhysRevLett.122.222001 [arXiv:1904.03947 [hep-ex]].

[12] S. Weinberg, Phys. Rev. **130**, 776-783 (1963) doi:10.1103/PhysRev.130.776

[13] S. Abreu, J. Dormans, F. Febres Cordero, H. Ita and B. Page, Phys. Rev. Lett. **122**, no.8, 082002 (2019) doi:10.1103/PhysRevLett.122.082002 [arXiv:1812.04586 [hep-ph]].

[14] P. Adlarson *et al.* [WASA-at-COSY], Phys. Rev. C **90**, no.3, 035204 (2014) doi:10.1103/PhysRevC.90.035204 [arXiv:1408.4928 [nucl-ex]].

[15] J. Z. Bai *et al.* [BES], Phys. Rev. Lett. **91**, 022001 (2003) doi:10.1103/PhysRevLett.91.022001 [arXiv:hep-ex/0303006 [hep-ex]].

[16] M. Ablikim *et al.* [BESIII], Chin. Phys. C **34**, 421 doi:10.1088/1674-1137/34/4/001 [arXiv:1001.5328 [hep-ex]].

[17] J. P. Alexander *et al.* [CLEO], Phys. Rev. D **82**, 092002 (2010) doi:10.1103/PhysRevD.82.092002 [arXiv:1007.2886 [hep-ex]].

[18] M. Ablikim *et al.* [BESIII], Phys. Rev. Lett. **108**, 112003 (2012) doi:10.1103/PhysRevLett.108.112003 [arXiv:1112.0942 [hep-ex]].

[19] J. Haidenbauer, EPJ Web Conf. **181**, 01028 (2018) doi:10.1051/epjconf/201818101028

[20] A. Datta and P. J. O'Donnell, Phys. Lett. B **567** (2003), 273-276 doi:10.1016/j.physletb.2003.06.050 [arXiv:hep-ph/0306097 [hep-ph]].

[21] G. J. Ding and M. L. Yan, Phys. Rev. C **72** (2005), 015208 doi:10.1103/PhysRevC.72.015208 [arXiv:hep-ph/0502127 [hep-ph]].

[22] B. A. Li, Phys. Rev. D **74** (2006), 034019 doi:10.1103/PhysRevD.74.034019 [arXiv:hep-ph/0510093 [hep-ph]].

[23] X. G. He, X. Q. Li, X. Liu and J. P. Ma, Eur. Phys. J. C **49** (2007), 731-736 doi:10.1140/epjc/s10052-006-0129-y [arXiv:hep-ph/0509140 [hep-ph]].

[24] B. S. Zou and H. C. Chiang, Phys. Rev. D **69** (2004), 034004 doi:10.1103/PhysRevD.69.034004 [arXiv:hep-ph/0309273 [hep-ph]].

[25] B. Loiseau and S. Wycech, Phys. Rev. C **72** (2005), 011001 doi:10.1103/PhysRevC.72.011001 [arXiv:hep-ph/0501112 [hep-ph]].

[26] A. Sibirtsev, J. Haidenbauer, S. Krewald, U. G. Meissner and A. W. Thomas, Phys. Rev. D **71** (2005), 054010 doi:10.1103/PhysRevD.71.054010 [arXiv:hep-ph/0411386 [hep-ph]].

[27] M. Röder *et al.* [COSY-TOF], Eur. Phys. J. A **49**, 157 (2013) doi:10.1140/epja/i2013-13157-9 [arXiv:1305.0451 [nucl-ex]].

[28] J. Haidenbauer, X. W. Kang and U. G. Meißner, Nucl. Phys. A **929**, 102-118 (2014) doi:10.1016/j.nuclphysa.2014.06.007 [arXiv:1405.1628 [nucl-th]].

[29] M. Ablikim *et al.* [BES], Phys. Rev. D **80**, 052004 (2009) doi:10.1103/PhysRevD.80.052004 [arXiv:0905.1562 [hep-ex]].

[30] M. Ablikim *et al.* [BES], Eur. Phys. J. C **53**, 15-20 (2008) doi:10.1140/epjc/s10052-007-0467-4 [arXiv:0710.5369 [hep-ex]].

[31] M. Ablikim *et al.* [BESIII], Phys. Rev. D **93**, no.5, 052010 (2016) doi:10.1103/PhysRevD.93.052010 [arXiv:1512.08197 [hep-ex]].

[32] S. B. Athar *et al.* [CLEO], Phys. Rev. D **73**, 032001 (2006) doi:10.1103/PhysRevD.73.032001 [arXiv:hep-ex/0510015 [hep-ex]].

[33] M. Z. Wang *et al.* [Belle], Phys. Rev. Lett. **92**, 131801 (2004) doi:10.1103/PhysRevLett.92.131801 [arXiv:hep-ex/0310018 [hep-ex]].

[34] M. Ablikim *et al.* [BES], Phys. Rev. Lett. **95**, 262001 (2005) doi:10.1103/PhysRevLett.95.262001 [arXiv:hep-ex/0508025 [hep-ex]].

[35] M. Ablikim *et al.* [BESIII], Phys. Rev. Lett. **106**, 072002 (2011) doi:10.1103/PhysRevLett.106.072002 [arXiv:1012.3510 [hep-ex]].

[36] M. Ablikim *et al.* [BESIII], Phys. Rev. Lett. **107**, 182001 (2011) doi:10.1103/PhysRevLett.107.182001 [arXiv:1107.1806 [hep-ex]].

[37] M. Ablikim *et al.* [BESIII], Phys. Rev. D **88**, no.9, 091502 (2013) doi:10.1103/PhysRevD.88.091502 [arXiv:1305.5333 [hep-ex]].

[38] M. Ablikim *et al.* [BESIII], Phys. Rev. Lett. **115**, no.9, 091803 (2015) doi:10.1103/PhysRevLett.115.091803 [arXiv:1506.04807 [hep-ex]].

[39] M. Ablikim *et al.* [BESIII], Phys. Rev. Lett. **117**, no.4, 042002 (2016) doi:10.1103/PhysRevLett.117.042002 [arXiv:1603.09653 [hep-ex]].

[40] M. Ablikim *et al.* [BESIII], Phys. Rev. D **97**, no.5, 051101 (2018) doi:10.1103/PhysRevD.97.051101 [arXiv:1801.02127 [hep-ex]].

[41] X. W. Kang, J. Haidenbauer and U. G. Meißner, Phys. Rev. D **91**, no.7, 074003 (2015) doi:10.1103/PhysRevD.91.074003 [arXiv:1502.00880 [nucl-th]].

[42] Y. F. Liu and X. W. Kang, Symmetry **8**, no.3, 14 (2016) doi:10.3390/sym8030014

[43] M. Ablikim *et al.* (BESIII Collaboration), Nucl. Instrum. Meth. A 614, 345 (2010).

[44] C. H. Yu *et al.*, Proceedings of IPAC2016, Busan, Korea, 2016, doi:10.18429/JACoW- IPAC2016-TUYA01.

[45] M. Ablikim *et al.* (BESIII Collaboration), Chin. Phys. C 44, 040001 (2020).

[46] X. Li et al., Radiat. Detect. Technol. Methods 1, 13 (2017); Y. X. Guo et al., Radiat. Detect. Technol. Methods 1, 15 (2017); P. Cao et al., Nucl. Instrum. Meth. A 953, 163053 (2020).

[47] S. Agostinelli *et al.* (Geant4 Collaboration), Nucl. Instrum. Meth. A 506, 250 (2003).

[48] S. Jadach, B. F. L. Ward and Z. Was, Comp. Phys. Commu. 130, 260 (2000); Phys. Rev. D 63, 113009 (2001).

[49] D. J. Lange, Nucl. Instrum. Meth. A 462, 152 (2001); R. G. Ping, Chin. Phys. C 32, 599 (2008).

[50] J. C. Chen et al., Phys. Rev. D 62, 034003 (2000).

[51] K. A. Olive *et al.* (Particle Data Group) Chin. Phys. C 38, 090001 (2014).

[52] https://hnbes3.ihep.ac.cn//HyperNews/get/AUX/2011/07/29/13.27-21355-ppb_v4.pdf

[53] https://indico.ihep.ac.cn/event/8006/contributions/99144/attachments/52883/60932/Trk4180.pdf

[54] M. Ablikim et al. (BESIII Collaboration), [arXiv:2111.07571 [hep-ex]].

[55] P. A. Zyla *et al.* (Particle Data Group), PTEP **2021**, 083C01 (2021).

[56] M. Gronau, J. L. Rosner and C. G. Wohl, Phys. Rev. D **97**, no.11, 116015 (2018) doi:10.1103/PhysRevD.97.116015 [arXiv:1808.03720 [hep-ph]].

[57] https://indico.ihep.ac.cn/event/11274/contributions/9410/attachments/4574/5197/gnnbar_light_hadron.pdf

8   Check for fitting method

The 100 times toy MC samples are generated by using our fitting results, and are used to perform IO check. The outputs of mass and width is consistent with input values within 1 σ, as shown Figure 35.
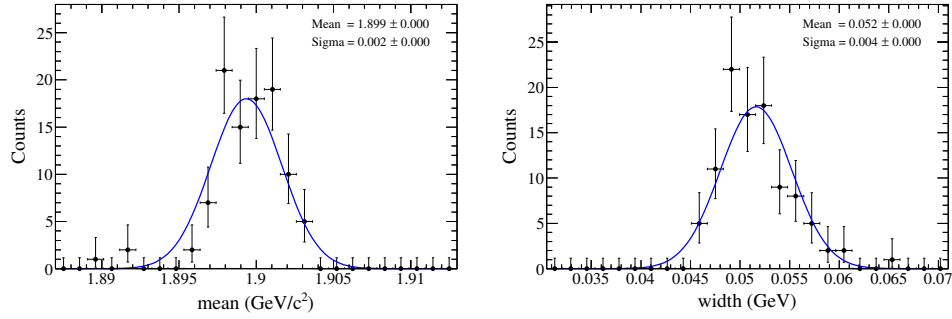
Fig. 35: The mass and width distributions for 100 times IO check by performing fit.

9 Appendices

9.1 Efficiency Correction

There is a difference between the efficiency of Monte Carlo and the efficiency of data. We use the control samples of processes $J/\psi \to p\pi^-\bar{n}$ and $J/\psi \to \bar{p}\pi^+n$ to calibrate this difference. We divid these selections into three categories: BDT selection, EMC selection, and TOF selection, as shown in Table 29. We take the number of events as the denominator before applying selections of BDT, EMC, and TOF, and the number of events as the numerator after applying selections of BDT, EMC, and TOF. So, we can further calculate the selection efficiency corresponding to various selections.

Tab. 29: Numerator and Denominator of Efficiency

Part	Sample selections	BDT/EMC/TOF selection
BDT	$R_{xy} < 0.6$	n_n_shower > 0
EMC	$R_{xy} < 0.6$ n_n_shower > 0	maximum deposition energy < 0.19 GeV
TOF	$R_{xy} < 0.6$ n_n_shower > 0 maximum deposition energy < 0.19 GeV	$T_{\text{tof}} - T_{\text{s}} - T_{\text{p}} \in (2,7.6) \,\|\, (8.5,15)$ ns

R_{xy}, the closest approaches of the tracks of p and π^- ($\bar{p}$ and π^+) to the interaction point, is used to suppress the background in the control sample. The variable n_n_shower is the number of showers selected by the requirement of BDT classifier. The maximum deposition energy means maximum energy of shower in the EMC after excluding neutron, and anti-neutron candidates, which is required to be less than 0.19 GeV. The seletion of flight time is required to be within $T_{\text{tof}} - T_{\text{s}} - T_{\text{p}} \in (2,\ 7.6)$ or $\in (8.5,\ 15)$ ns. They are same as our selections of signal process $J/\psi \to \gamma n\bar{n}$,

The calculation of efficiency is divided into two dimensions: momentum magnitude and emission angles. The momentum magnitude is divided into 5 bin from 0.2 to 1.2 GeV/c, and the emission angle is divided into 8 bin from -0.8 to 0.8. At the same time, the number of events for each bin is also calculated, which can be used to obtain our efficiency graph.
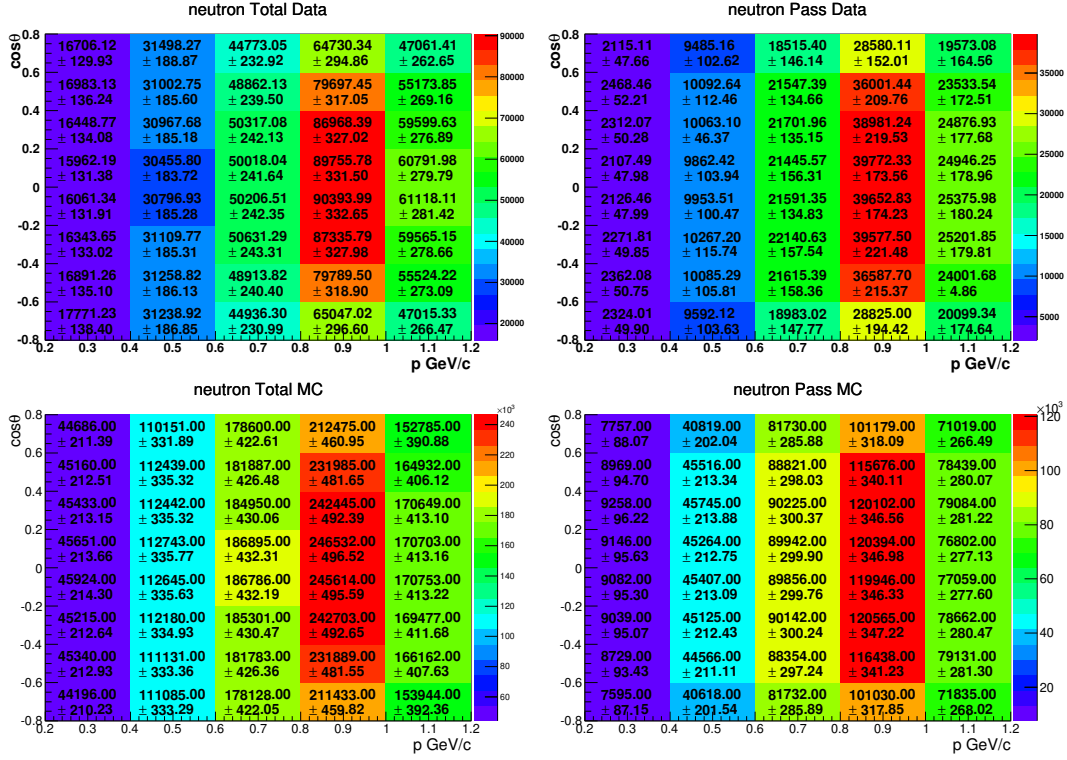
684 **9.1.1 BDT**

Fig. 36: The neutron counts in different bins of momentum magnitude and emission angles before(left) and after(right) applying the BDT selection for data(top two) and MC(bottom two).
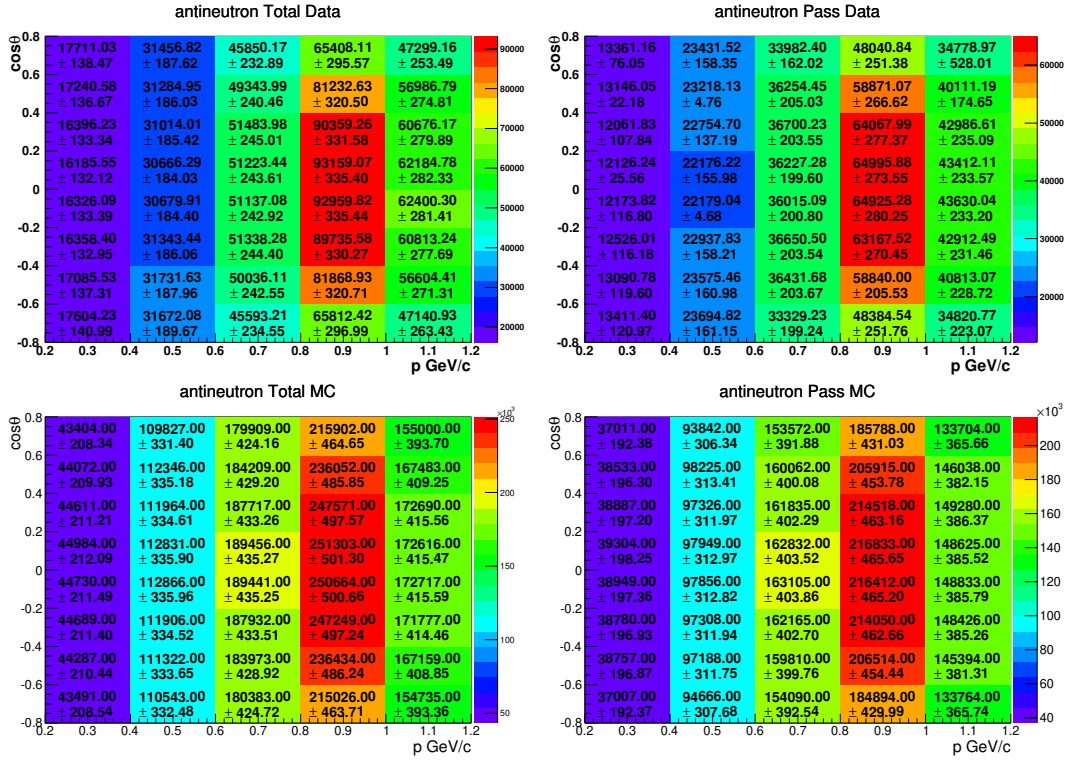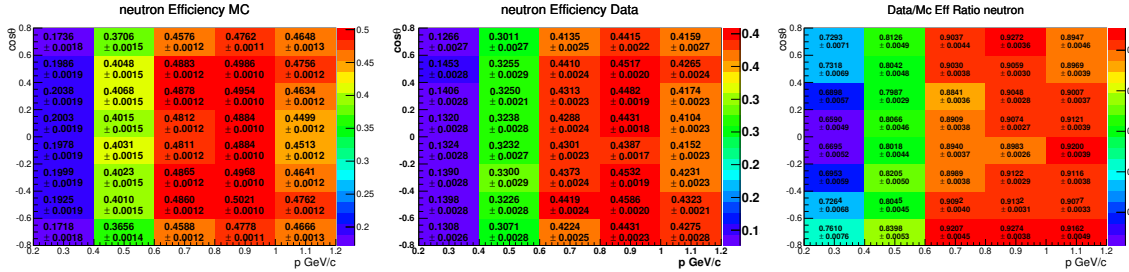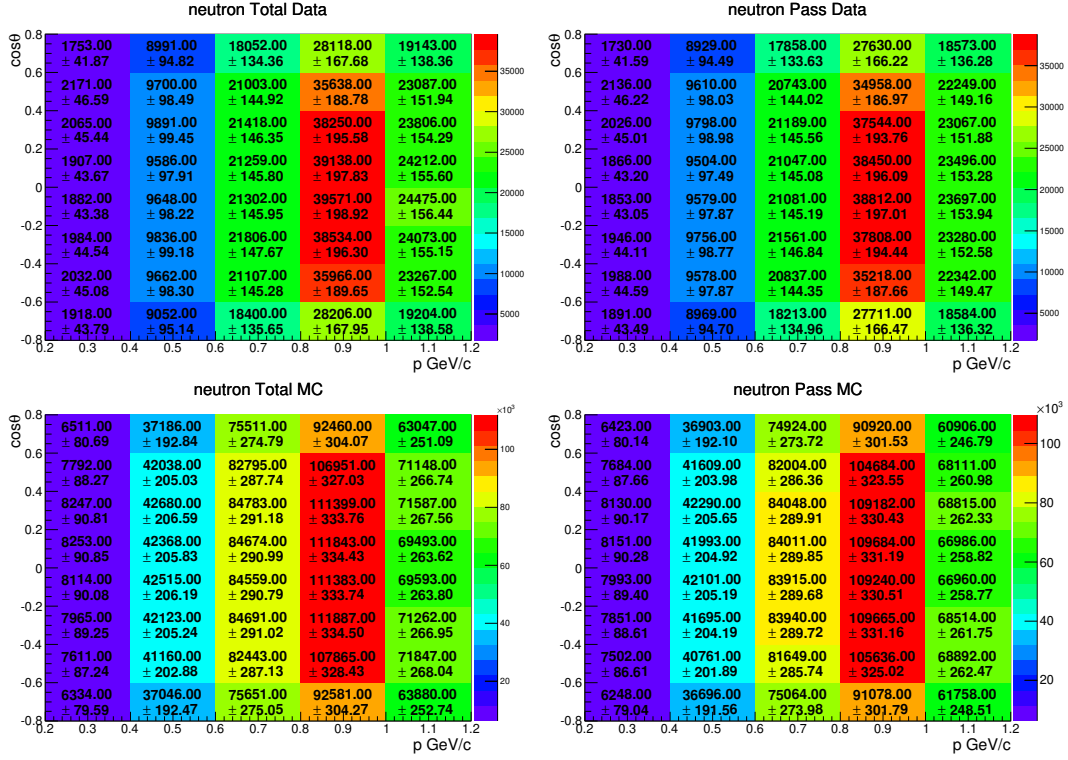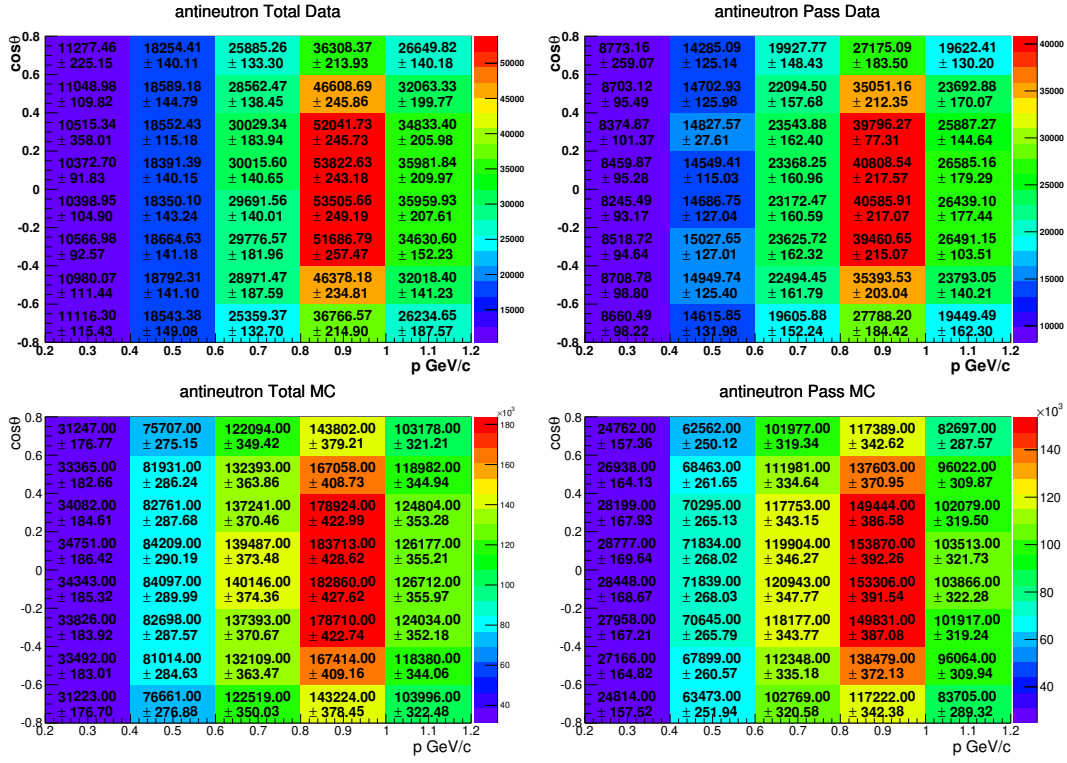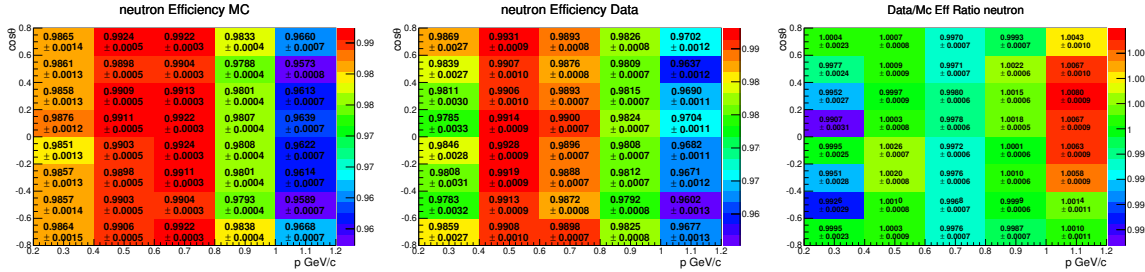
Fig. 37: The anti-neutron counts in different bins of momentum magnitude and emission angles before(left) and after(right) applying the BDT selection for data(top two) and MC(bottom two).

Fig. 38: Efficiency of neutrons in different bins of momentum magnitude and emission angles. For MC simulation(left), data(middle), Data/MC efficiency ratio(right).
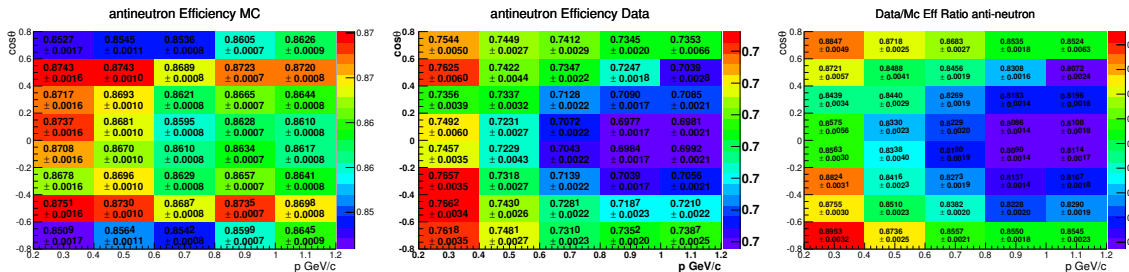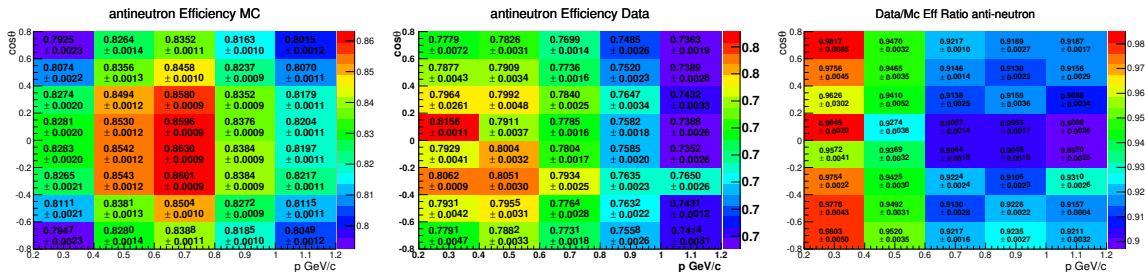

Fig. 39: Efficiency of anti-neutrons in different bins of momentum magnitude and emission angles. For MC simulation(left), data(middle), Data/MC efficiency ratio(right).

685   **9.1.2   EMC**

Fig. 40: The neutron counts in different bins of momentum magnitude and emission angles before(left) and after(right) applying the EMC selection for data(top two) and MC(bottom two)
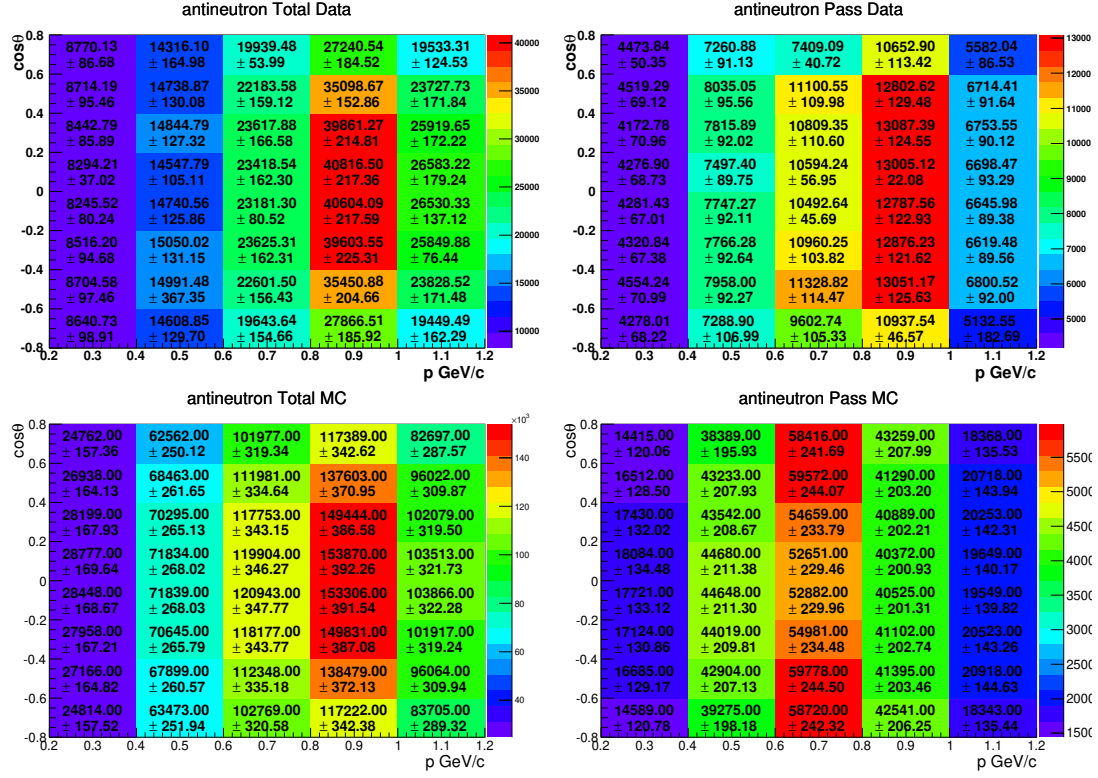
Fig. 41: The anti-neutron counts in different bins of momentum magnitude and emission angles before(left) and after(right) applying the EMC selection for data(top two) and MC(bottom two).
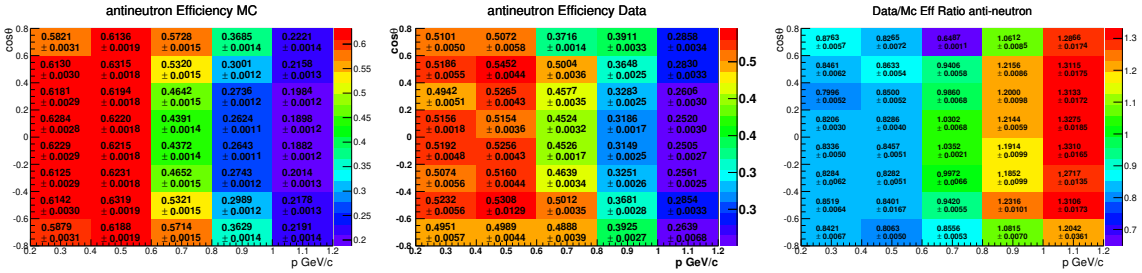

Fig. 42: Efficiency of neutrons in different bins of momentum magnitude and emission angles. For MC simulation(left), data(middle), Data/MC efficiency ratio(right).

Fig. 43: Efficiency of anti-neutrons in different bins of momentum magnitude and emission angles. For MC simulation(left), data(middle), Data/MC efficiency ratio(right).

686 **9.1.3 TOF**

Fig. 44: The anti-neutron counts in different bins of momentum magnitude and emission angles before(left) and after(right) applying the EMC selection for data(top two) and MC(bottom two).

Fig. 45: Efficiency of anti-neutrons in different bins of momentum magnitude and emission angles. For MC simulation(left), data(middle), Data/MC efficiency ratio(right).

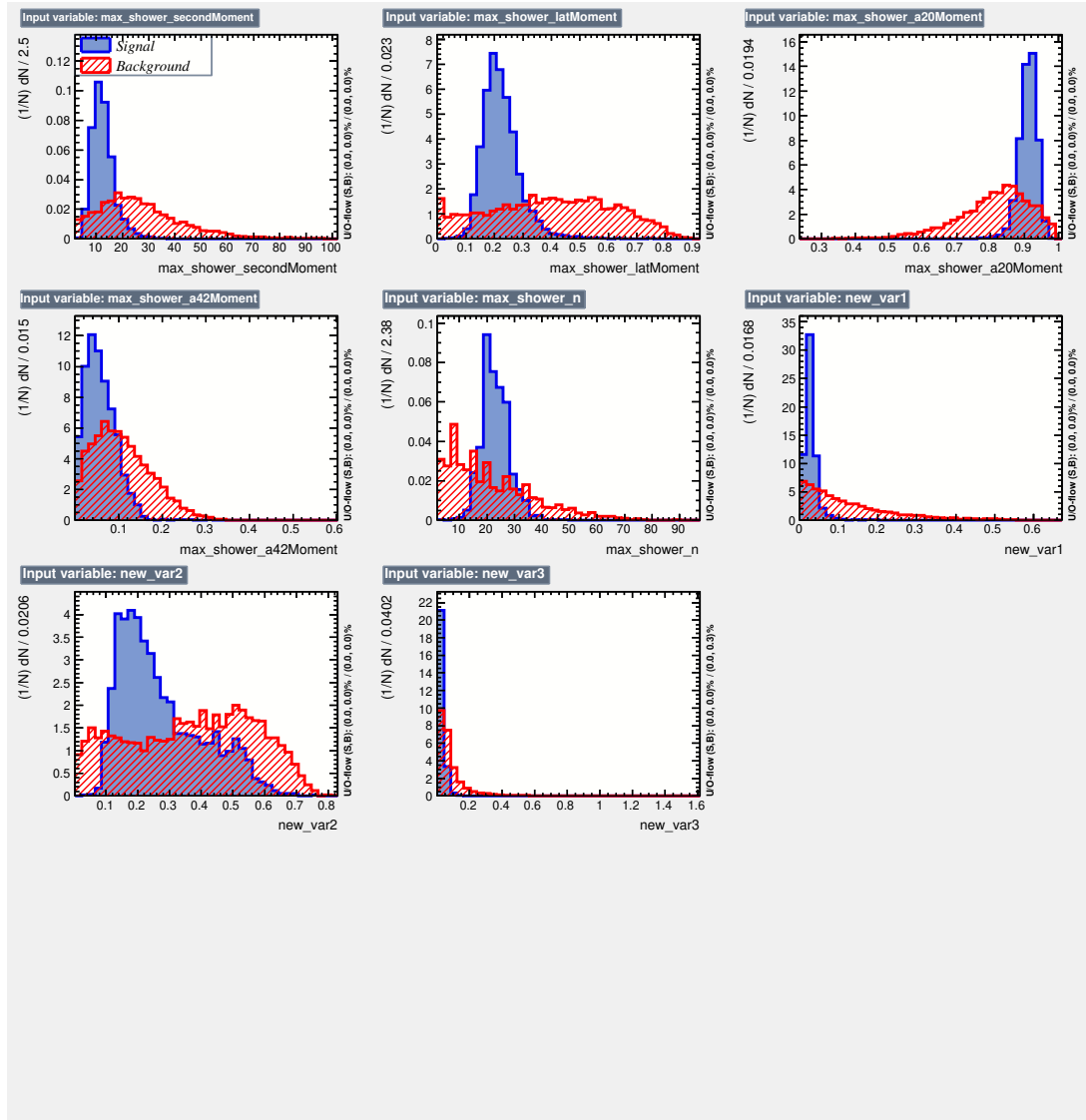## 10 The distributions for each variables used in the MVA analysis

Fig. 46: The distributions for each variables used in the MVA analysis related to the signal (γ) and background ($n\bar{n}$) samples used for the training.
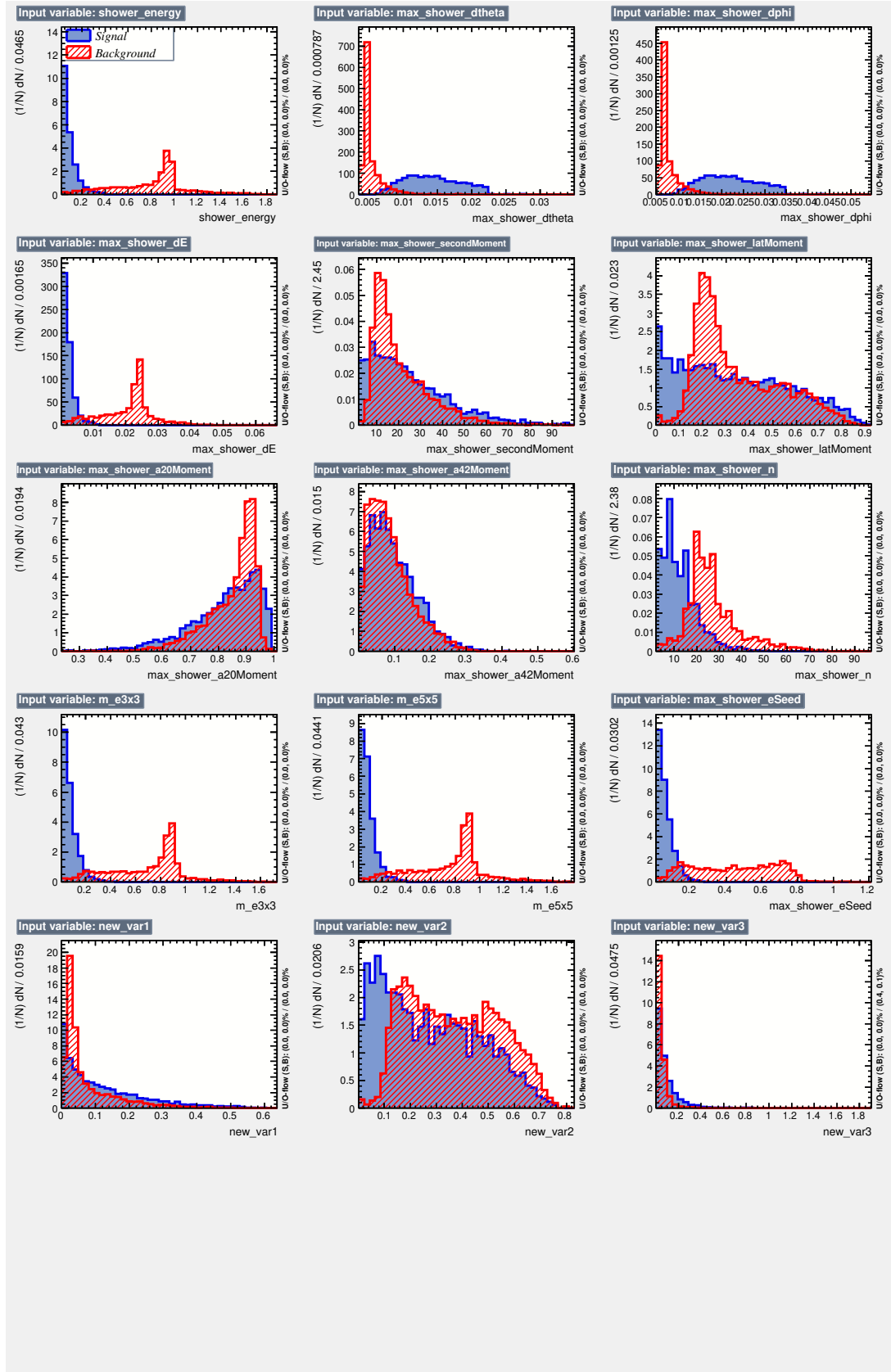
Fig. 47: The distributions for each variables used in the MVA analysis related to the signal (*n*) and background ($\gamma\bar{n}$) samples used for the training.
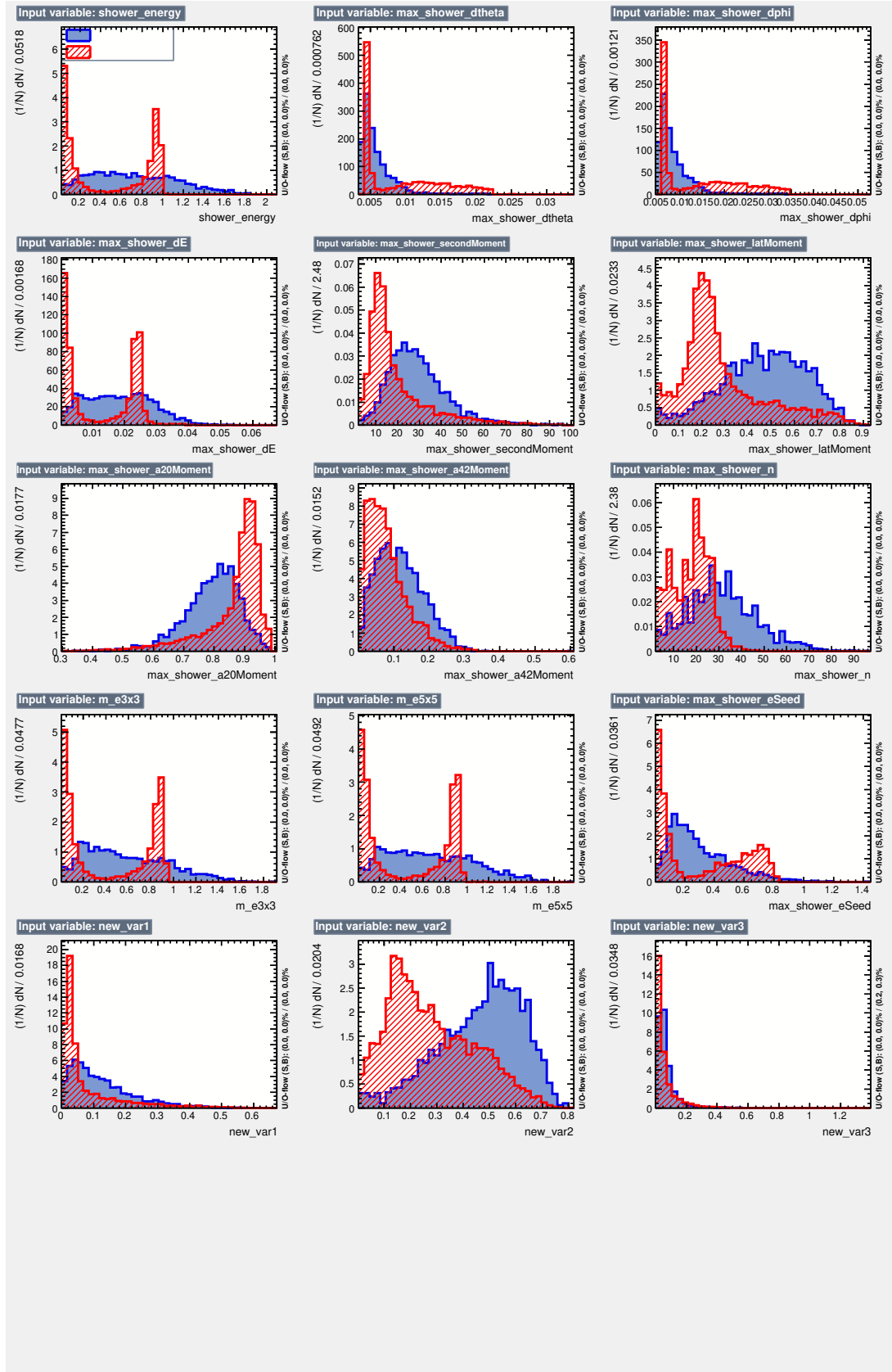
Fig. 48: The distributions for each variables used in the MVA analysis related to the signal ($\bar{n}$) and background (γn) samples used for the training.

11 The distributions of multiple variable for control samples

We compared the distributions of multiple variable (BDT variables) using control samples, as shown in Figure 49 and Figure 50.
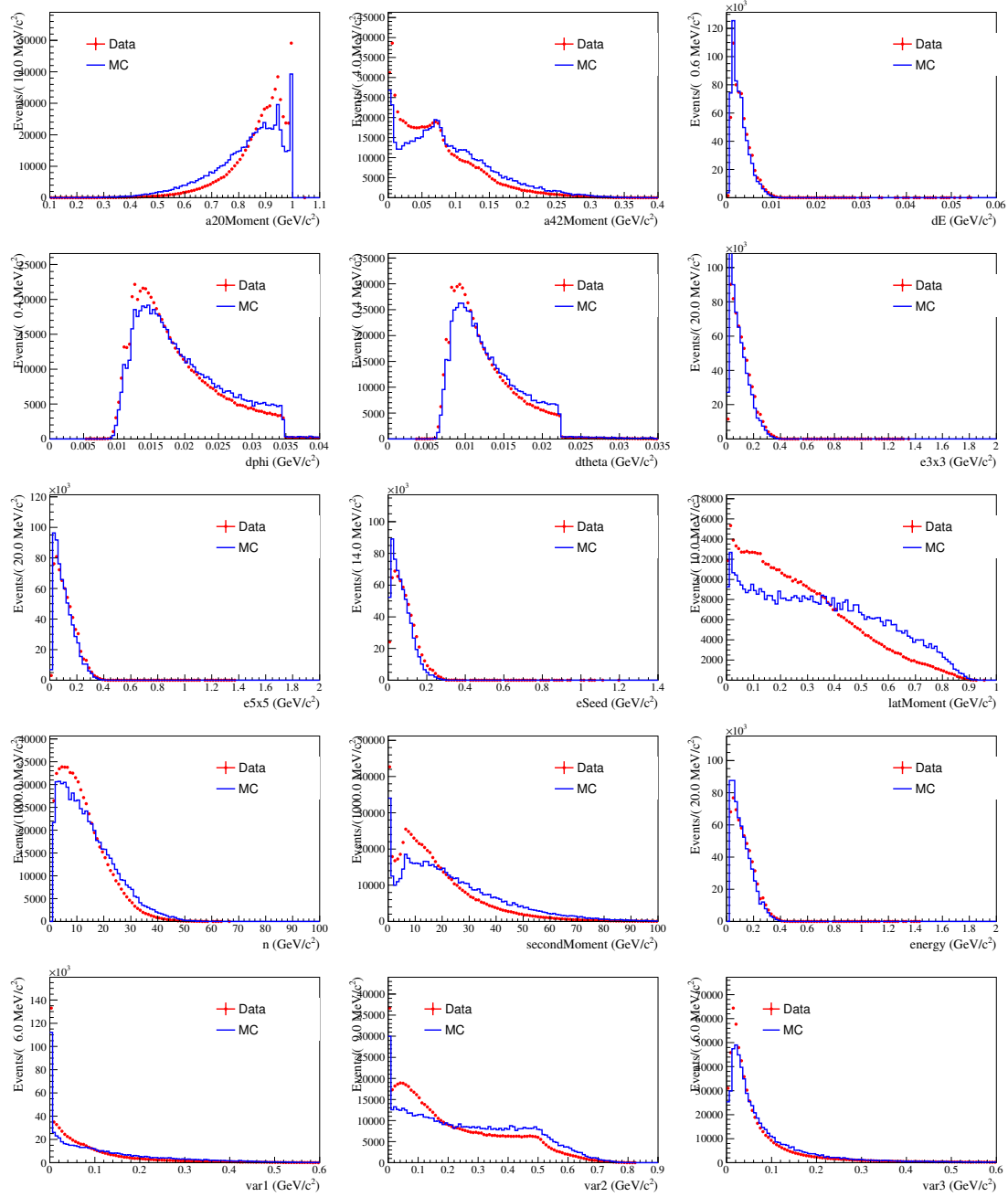

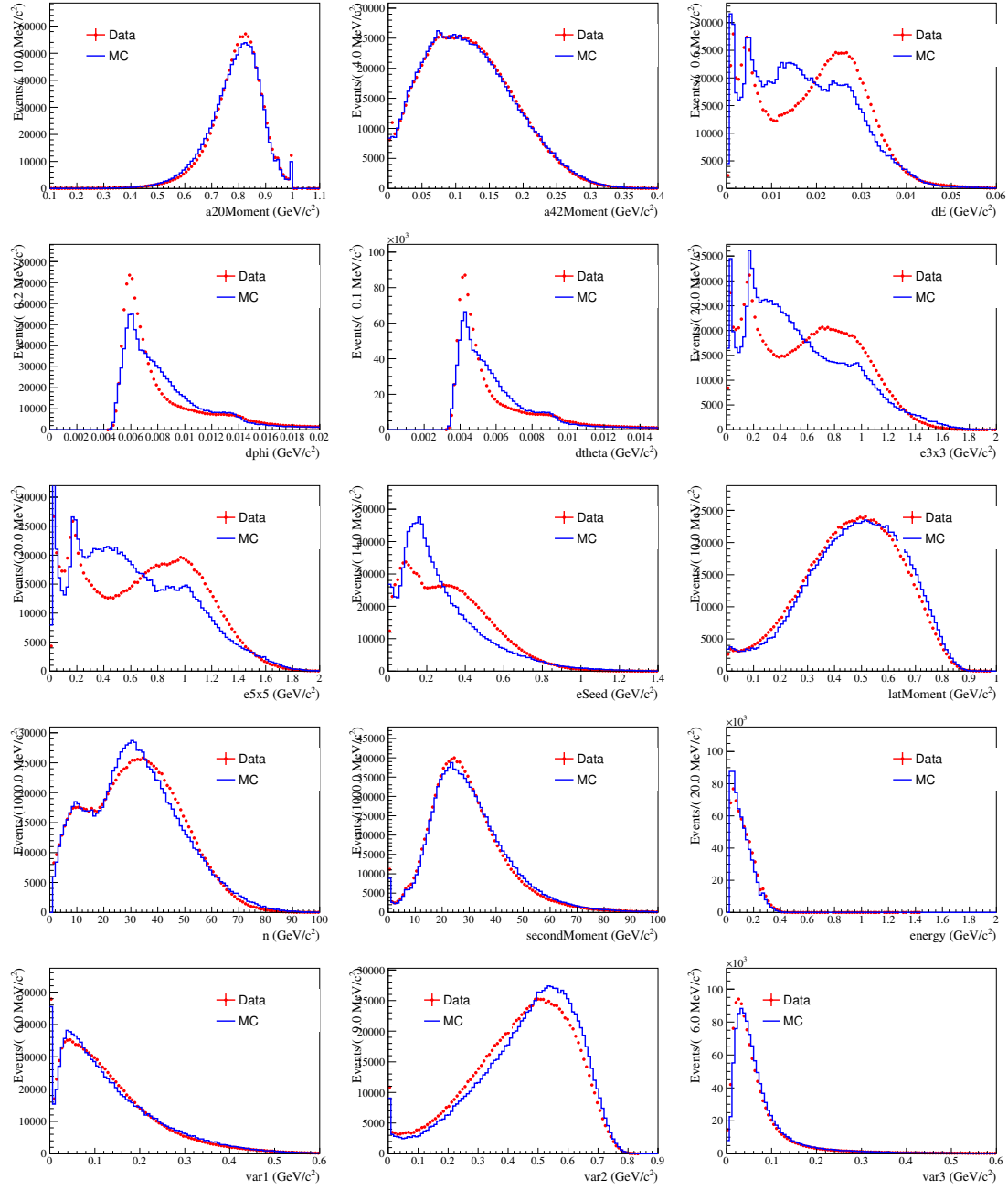Fig. 49: The distributions of multiple variable between data and MC for control sample $J/\psi \rightarrow \bar{p}n\pi^{+}$.

Fig. 50: The distributions of multiple variable between data and MC for control sample $J/\psi \to p\bar{n}\pi^-$.